Memoirs of the School of Engineering, Nagoya University
Vol.44. No.2 (1992)

IMPROVEMENT OF CORONA-PREIONIZED TEA-CO_2 LASER AND ITS APPLICATION TO NON-DESTRUCTIVE AND REMOTE INSPECTION

Keiji NAKAMURA, Chobei YAMABE and Kenji HORII*

Department of Electrical Engineering

(Received November 9, 1992)

Abstract

This paper describes the improvement of a corona-preionized TEA-CO_2 laser and its application to non-destructive and remote inspection of an electric suspension insulator. The laser output energy was increased by superposing a high-frequency corona discharge (HFCD) on the main discharge due to the suppression of glow-to-arc transition even for the input energy density over 200 J/l. The HFCD was also produced without another power supply by using the SC-HFCD circuit, in which the residual energy not to be injected into the main discharge volume was recycled as the energy source of the HFCD in the next laser operation. Furthermore the TEA-CO_2 laser was utilized as a vibrational source, and the natural vibration of an electric insulator was excited. The dependence of the vibrational amplitude on the irradiation intensity was explained by the model combining the vibrational principles of thermal shock, reaction of spouting particles and the spherical shock wave. It was comfirmed that a cracked insulator can be distinguished from a normal one by detecting the change of the natural vibration due to the crack.

1. Introduction

A corona-preionized TEA-CO_2 laser has a relatively simple structure and a good ability for efficiency and lifetime in a sealed-off operation. This is because the energy for the preionization is so small that the laser gas is not so degraded due to few impurities produced from the preionizer[1]. However it is difficult to increase the electrical input energy density in the main discharge volume over 200 J/l, because the intensity of the corona preionization is relatively weak as compared with that of the other preionization source, UV sparks and

*Toyota College of Technology

X-ray. This is the reason why the corona preionization is not used for a high-power laser system. It has been just desirable to enlarge the extractable energy of corona-preionized TEA-CO_2 lasers in order to make use of such superior features, and various techniques to increase the corona preionization intensity has been developed. Ernst[2)-5)] achieved the input energy density over 200 J/l with the efficiency of 18.5% both to intensify the corona preionization due to the rapid application of high voltage and to uniform the electric field on the cathode with Ernst profile[6)]. Yamabe et al.[7)] have been reported that the extractable energy of corona-preionized TEA-CO_2 laser can be increased by superposing a high-frequency corona discharge (HFCD) on main discharge, although they examined the effect of HFCD only for the input energy density less than 200 J/l.

On the other hand, a laser beam has recently attracted an attention as a new media for non-destructive and remote inspection because of more convenience of a laser device than radioactive sources. Also, a laser beam which has both a good directivity and a long interferable length is preferable for a remote inspection. The two different types of laser inspection have been reported[8),9)]. One is the detection of the ultrasound generated by a high-power pulsed laser with a laser interferometer[10),11)]. The depth of a slot on an aluminum block was estimated by the arrival difference time between the shear pulse and the Reyleigh pulse. The other is the detection of the change of the periodical vibration with the irradiating frequency of the incident laser beam[12)-15)]. The drilled holes of 0.8 mm diameter in an aluminum block can be detected due to a phase decay of 5 degrees. However there are the following problems in these techniques in a practical application. For the former method, not only the interferometer with upper limit frequency over 15 MHz is necessary but it is difficult to realized the signals due to the defects in a article with a complicated shape. For the latter method the use of a lock-in amplifier and the scanning of the laser beam lead to the prolongation of working hours.

One purpose of the present study is to increase the input energy density of corona-preionized TEA-CO_2 lasers over 200 J/l by superposing a HFCD on the main discharge as reported by Yamabe et al.[7)], and it is examined how effect on the discharge condition and optical energy extraction the HFCD have. Further the new circuit called as SC-HFCD circuit is devised to miniaturize the laser device with the HFCD circuit, and the characteristics of main discharge and laser output are measured. The results are included the former half of this paper.

The other purpose of the present study is to apply the TEA-CO_2 laser to a vibrational source of electric suspension insulators and to examine a new inspection to distinguish a cracked insulator detecting the sound of natural vibration, whose the frequency components and the decay time changes due to the cracks in the insulator. Although various informations of the cracks can be realized by using the techniques described before, it is sufficiently useful in some applications to find only whether some cracks are in the solid sample. The inspection method to detect the natural vibration has the following advantages:

(1) A cracked insulator can be detected with a single laser operation using an interferometer because the efficient energy conversion from the laser beam to the vibration of the insulator makes the acoustic signal generated clearly. Therefore it is expected to inspect the insulator without a lock-in amplifier and to save the inspecting time.

(2) There are no particular restrictions for the shape and the size of the insulator because the cracked insulator can be distinguished by detecting the change of the natural vibration for the frequency components or the duration of the natural vibration.

A lineman has to go up over several-ten meters above the ground and directly touches the insulators with a specific instrument as usual in order to test them on the practual high voltage transmission lines. However, it is necessary to check the insulators remotely in order both to improve the reliability and the safety of the test and to save the working time. It is considered

that the inspecting system described in this chapter is the effective method for such a demand because a laser beam has the characteristics of remote sensing with a good directivity and a long interferable length. The author has studied on the possibility that the existence of crack can be realized by performing Fast Fourier Transfer (FFT) to the vibrational signal detected with a laser interferometer or hearing the sound of the vibrational signal. The results are included in the latter half of this paper.

The present paper consists of the following chapters.

In chapter 2, the effects of HFCD on the main discharge and the output performance in a corona-preionized TEA-CO_2 laser are described. It is shown that the output energy density increases by means of HFCD due to the suppression of the glow-to-arc transition and that some conditions for the HFCD current is required to be satisfied in order to increase the laser output.

In chapter 3, the effects of SC-HFCD circuit on the laser and discharge performance are described. The PFN parameters are optimized so that the inefficient energy not to be injected into the discharge volume can be collected by SC-HFCD circuit without the remarkable decrease of the laser output, and HFCD can be superposed on the main discharge without supplying the extra-energy for the HFCD operation from another power source. It is shown that the laser output is improved and that the operating voltage in the SC-HFCD circuit is determined by the amounts of electrical charge flowing into and out of the SC-HFCD circuit.

In chapter 4, the vibrational characteristics of an electric suspension insulator with the irradiation of pulsed CO_2 laser beam on the surface of the insulator is described. It is shown that the reaction of particles spouting from the insulator chiefly makes the insulator vibrated.

In chapter 5, the non-destructive and remote inspection system for an electric suspension insulator using a pulsed TEA-CO_2 laser to vibrate the insulator and a laser interferometer to detect the vibration remotely is described. It is shown that the crack in the insulator is realized by performing FFT to the detected vibrational signal or by hearing the sound of the signal.

In chapter 6, the content of the present paper is summarized.

2. Improvement of Corona-Preionized TEA-CO_2 Laser by Means of High Frequency Corona Discharge

2. 1. Experimental Apparatus and Procedure

The electrical circuit of the experimental apparatus is shown in Fig. 2. 1. The main electrodes, 50 mm wide and 600 mm long, are made of aluminum at an interval of 30 mm. The effective discharge volume is estimated as 0.5(l). The anode is formed with the Chang profile[16] and the cathode has ten parallel grooves 4.5 mm wide and 3 mm deep on the surface along the laser axis. Many trapezoidal protrusions are distributed on the surface along the laser axis between each groove[17].

A trigger electrode covered with a pyrex glass tube is put in each groove. The outer diameter and the thickness of the glass tube are 4 mm and 1.2 mm, respectively.

The electrical discharge circuit with the pulse forming network (PFN) is composed of the capacitances C_1(=60 nF), C_2(=52 nF), the inductances L_1(=22.4 μH), L_2(~ 100 nH), and the gaps G_1, G_2 pressurized with nitrogen gas. The HFCD circuit is enclosed by the broken line in Fig. 2. 1, and the operating sequence of these circuits is described in 2. 2. 1 in detail. The

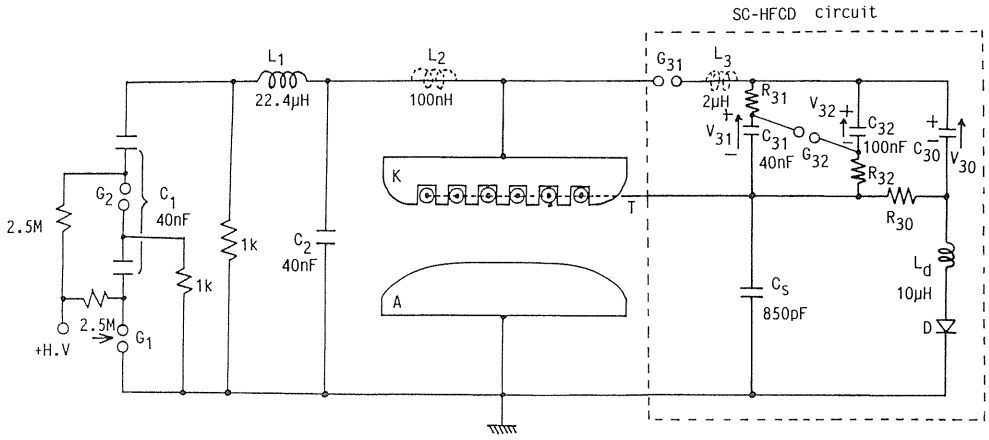

Fig. 2. 1. Schematic diagram of experimental apparatus and electrical circuit.

minimums of the inductances L_3 and L_s are 1.7 μH and 2.5 μH, respectively, due to the geometrical structure of the laser device.

A $CO_2/N_2/He$ mixture gas in the ratio 1:1:5(l/min) is flowed along the laser axis at atmospheric pressure. The optical resonator consists of a gold-coated reflector with a 10 m radius of curvature and a germanium flat coupler with a reflection coefficient of 51%. The length of the resonator is about 1 m.

The laser beam is partially reflected on the surface of the NaCl Brewster window, and the waveform of the laser output pulse is measured by detecting the reflected beam with a gold-doped germanium detector cooled by liquid nitrogen. The waveforms of the voltage V between the main electrodes and the main discharge current I_m are measured with a R-C divider and a search coil, respectively, while the waveform of the current at the trigger electrode, I_t, is measured with a Rogowski coil. The glow-to-arc transition rate is measured by timing the rapid reduction of V due to the arcing for the thirty discharges at the repetition rate of 0.1 Hz. The laser output is also measured with a calorimeter.

2. 2. *Experimental Results*

2. 2. 1. *Effect of Triggering Time of HFCD Current*

The waveforms of the voltage V, the main discharge current I_m, the laser power and the trigger current I_t are shown in Fig. 2. 2 when V_1=60 kV, V_3=20 kV, C_3=40 nF, C_s=850 pF, L_3=1.7 μH and L_s=2.5 μH, where V_1 and V_3 are the applied voltage on the capacitances C_1 and C_3, respectively. The breakdown voltage between the main electrodes and the peak value of I_m are about 55 kV and 3.5 kA, respectively. In the waveform of I_t, the trigger current passes through the capacitance C_s before the spark of G_3, and then the HFCD current flows by L-C oscillation at the trigger electrode through C_3 and L_3 after the spark of G_3. The peak value of the HFCD current ($\fallingdotseq$ 700 A) is so large that the main discharge volume is intensively preionized by the HFCD current. The time $t_{G3\text{-}BD}$ between the spark of G_3 and the main discharge indicates the delay time of the main discharge after the preionization, as shown in Fig. 2. 2.

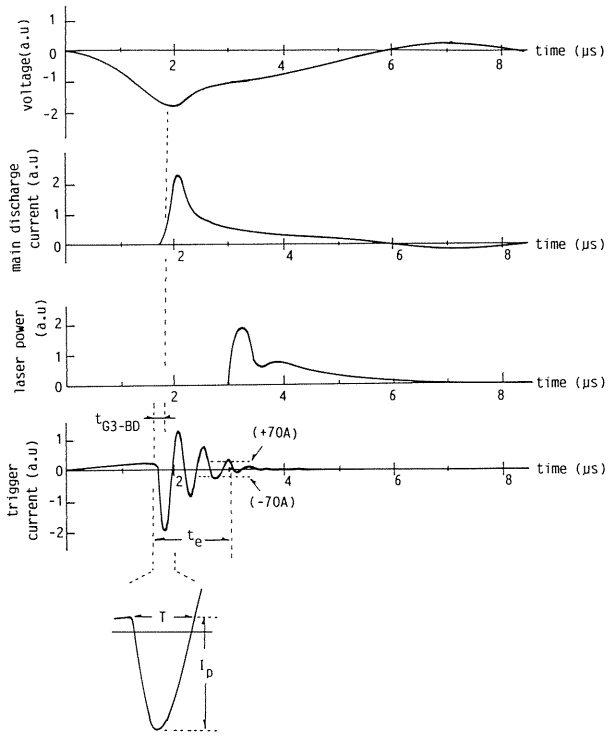

Fig. 2. 2. Temporal characteristics of voltage across the main electrodes, main discharge current, laser output power and trigger current. The definitions of delay time $t_{G3\text{-}BD}$, peak value I_p, half-period T and duration t_e are also shown in the bottom figure.

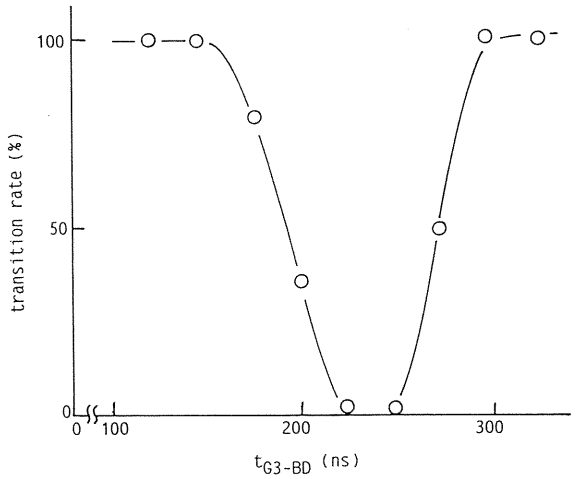

Fig. 2. 3. Transition rate as a function of delay time $t_{G3\text{-}BD}$.

Fig. 2. 3 shows the variation of the glow-to-arc transition rate with the delay time $t_{G3\text{-}BD}$. The operating parameters are V_1=58.8 kV, V_3=20 kV, C_3=40 nF, C_s=850 pF, L_3=1.7 μH and L_s=2.5 μH. There is an optimal value of $t_{G3\text{-}BD}$, 220 ns ~ 240 ns, for suppressing the glow-to-arc transition, and an arc-free discharge (zero transition rate) is maintained at the input energy density of about 205 J/l. A similar tendency is reproducibly observed at other operating parameters.

The delay time of the main discharge from the preionization has been reported in the refs.18, 19 and 20, however the reported values are longer than the values obtained in this experiment. All experimental results described below are obtained under the most suitable condition for the delay time of $t_{G3\text{-}BD}$.

2. 2. 2. *Characteristics of Laser Output with HFCD Circuit*

Fig. 2. 4 shows the relationship between the laser output and V_1 as a parameter of V_3 in the case of C_3=40 nF, L_3=1.7 μH, L_s=2.5 μH, and C_s=850 pF.

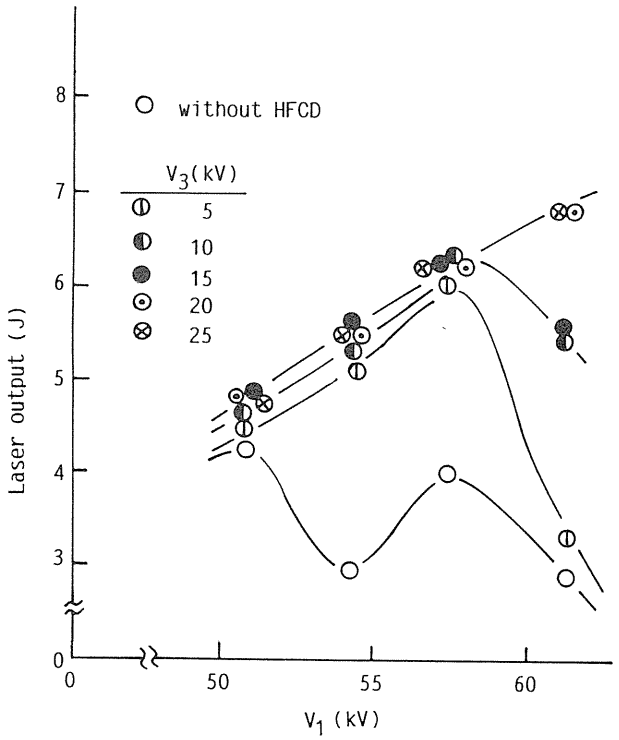

Fig. 2. 4. Relationship between laser output and voltage V_1 as a parameter of voltage V_3.

The laser output without the HFCD circuit is saturated at V_1 of about 51.3 kV and gradually decreases for $V_1 > 51.3$ kV because of the occurrence of the glow-to-arc transition, while that with the HFCD circuit is saturated at V_1 higher than 51.3 kV because of the suppression of the glow-to-arc transition due to the increase of the peak value of the HFCD

current with V_3. Arc-free discharges are produced for the input energy density up to about 205 J/l for $V_3 > 20$ kV, where the output energy density is about 13 J/l, as shown in Fig. 2. 3, while the output energy density of about 14 J/l is obtained at a transition rate of less than 10%, where the input energy is 220 J/l at V_1=60 kV. It is suggested that the HFCD circuit is effective for the increase of the laser output for the input energy density over 200 J/l, where the glow-to-arc transition would occur during the main discharge without the HFCD circuit. The waveforms of the voltage between the main electrodes and the main discharge current prior to the glow-to-arc transition are independent of the parameters in the HFCD circuit, so that the laser output depends only on the stability of the main discharge, i.e. the glow-to-arc transition rate.

2. 2. 3. *Effect of Parameters of C_3, C_s and L_3 in HFCD Circuit*

Fig. 2. 5 shows the relationship between the capacitance C_3 and the laser output, where V_1=60 kV, V_3=20 kV, C_s=850 pF, L_3=1.7 μH and L_3=2.5 μH. The laser output is saturated at a certain value of C_3.

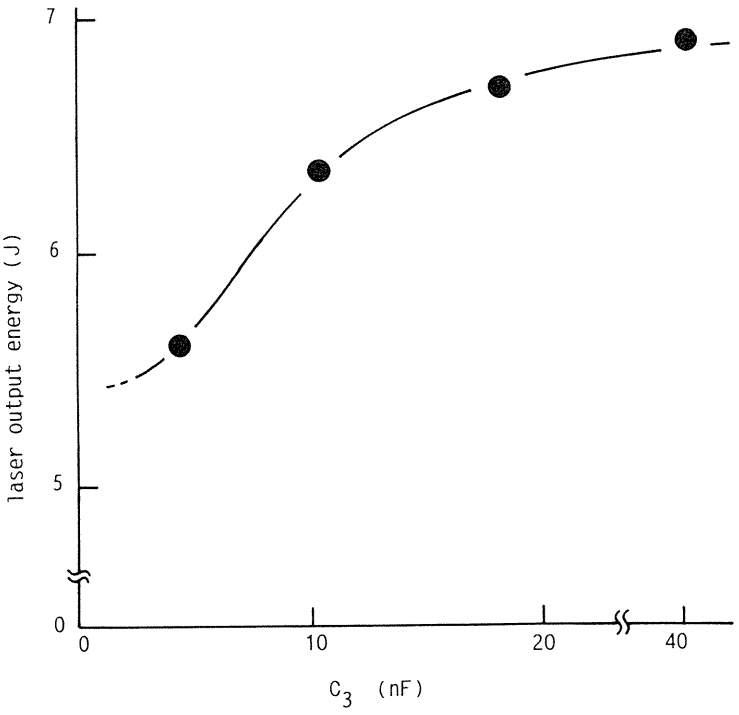

Fig. 2. 5. Variation of laser output with capacitance C_3.

Fig. 2. 6 shows the relationship between the inductance L_3 and the laser output as a parameter of V_3, where V_1=60 kV, C_3=40 nF, C_s=850 pF and L_s=2.5 μH. The laser output decreases with the increase of L_3, and it is found that the reduction of L_3 results in the increase of laser output.

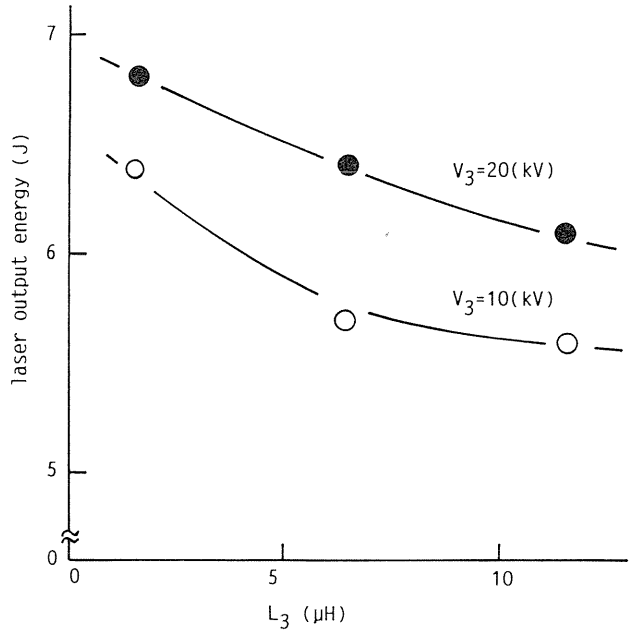

Fig. 2. 6. Variation of laser output with inductance L_3 as a parameter of voltage V_3.

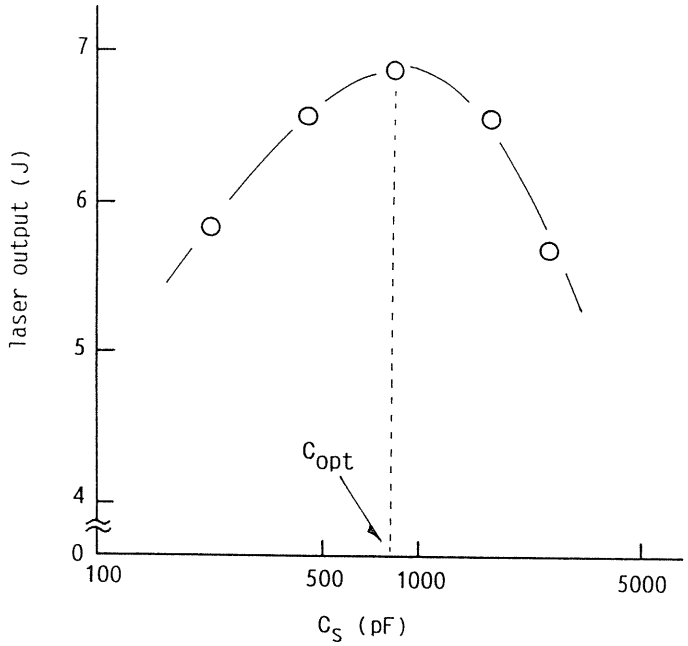

Fig. 2. 7. Variation of laser output with capacitance C_s.

Fig. 2. 7 shows the relationship between the capacitance C_s and the laser output, where V_1=60 kV, V_3=20 kV, C_3=40 nF, L_3=1.7 μH and L_s=2.5 μH. There is the optimal value of C_s, C_{opt}, to maximize the laser output.

These characteristics of the laser output is considered to depend on the waveform of HFCD current, and it is discussed in 2. 3. 1.

2. 3. Discussion

2. 3. 1. Influence of Waveform of HFCD Current on Laser Output

The waveform of HFCD current is characterized by peak value, period and duration. The influence of these factors on the laser output is examined on the basis of the previous experimental results.

I_p, T and t_e are defined as the peak value, the half-period and the duration of the HFCD current, respectively, as shown in Fig. 2. 2. Fig. 2. 8 shows the dependence of t_e on C_3 at V_1=60 kV, V_3=20 kV, C_s=850 pF, L_3=1.7 μH and L_s=2.5 μH, where both I_p and T do not change appreciably with C_3. The variation of t_e with C_3 considerably corresponds to that of the laser output shown in Fig. 2. 5. It is found that t_e of 1 ~ 1.5 μs at the saturation point of the laser output considerably agrees with the pulse width of the main discharge current from the peaking capacitance C_2. Therefore it seems to be important to produce the electrons on the surface of the cathode while the discharge current flows from C_2 at least.

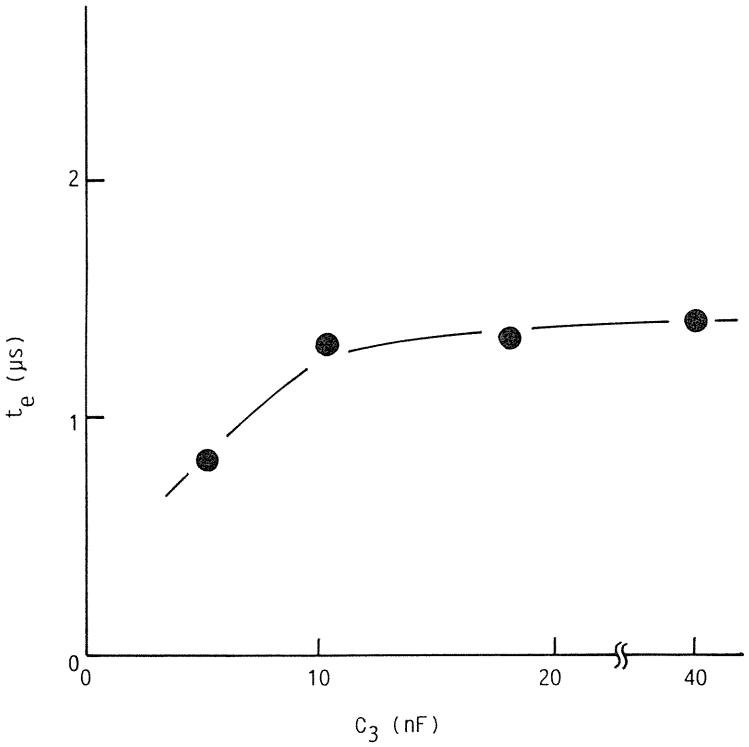

Fig. 2. 8. Dependence of duration t_e on capacitance C_3.

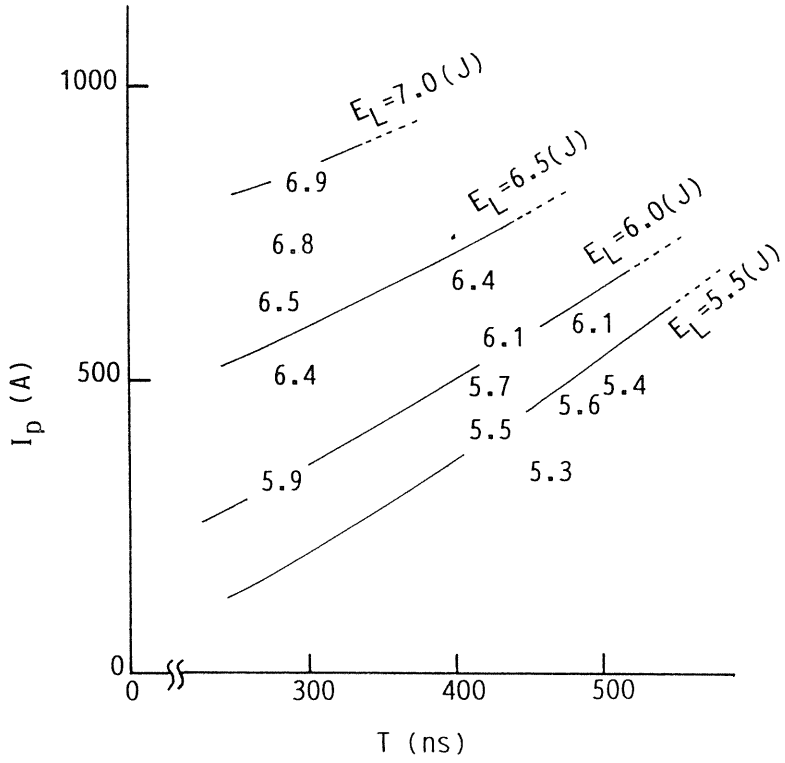

Fig. 2. 9. Contour lines of laser output as functions of peak value I_p and half-period T.

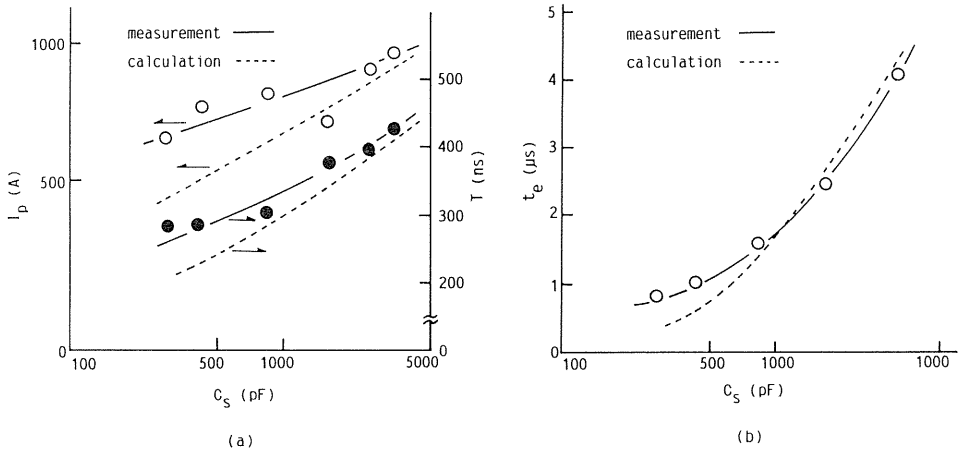

Fig. 2. 10. (a) Measured and calculated relationships between capacitance C_s and peak value I_p or half-period T.
(b) Measured and calculated relationships between capacitance C_s and duration t_e.

Fig. 2. 9 shows the contour lines of the laser output E_L with the changes of I_p and T using the experimental results shown in Figs. 2. 4 and 2. 6, where t_e is more than 1 μs. As shown in Fig. 2. 9, the laser output increases as I_p becomes higher or T becomes shorter with the increase of V_3 and with the decrease of L_3. Therefore short T and high I_p are very important, and it is necessary both to increase V_3 and to reduce L_3 in order to increase the laser output.

Fig. 2. 10 shows the observed variation of (a)I_p, T and (b)t_e with C_s. The period T is so large for $C_s > C_{opt}$, while t_e is less than 1 μs for $C_s < C_{opt}$. Therefore, there is the optimal value of C_s, C_{opt}, to maximize the laser output as shown in Fig. 2. 7.

2. 3. 2. *Mechanism of Suppression of Glow-to-Arc Transition with HFCD Operation*

Both the adjustment of $t_{G3\text{-}BD}$ and the shortness of T other than the highness of I_p lead to stabilize the main discharge due to the suppression of the glow-to-arc transition and to increase the laser output as described before. It is very important to ionize the whole discharge volume homogeneously and to suppress the filamentary streamer formation with a homogeneous layer of electrons formed by overlapping the electron avalanches for the suppression of the glow-to-arc transition[21),22)].

Here is estimated the relationship between the developing distance of the electron layer from the surface of the cathode and $t_{G3\text{-}BD}$ as well as T. Assuming that the distortion of the electric field by the spatial charges in the discharge volume can be neglected, the developing distance from the cathode, x, is approximately calculated using the drift velocity v_d in the laser mixture gas as follows[23)].

$$V_d = \begin{cases} 1.4 \cdot 10^6 \cdot (E/P) & \cdots\cdots (0 \leqq E/P \leqq 2) \\ 4.5 \cdot 10^5 \cdot (E/P) + 2 \cdot 10^6 & \cdots\cdots (2 \leqq E/P \leqq 20) \end{cases}, \qquad (2\text{-}1)$$

$$(V_d \text{ in cm}, E/P \text{ in } V/cm \cdot Torr)$$

$$x = \int_{t_1}^{t} v_d \, dt \qquad (x \text{ in cm}), \qquad (2\text{-}2)$$

where E is the electric field in the discharge volume, P is the total pressure of the laser mixture gas, and t_1 is the time when the electrons start from the cathode.

Fig. 2. 11 shows the relationship between x and t_1 when t is 1.9 μs, which is the time of the main discharge initiation, where the change in E before the main discharge is calculated for the circuit shown in Fig. 2. 1. When t_1 is 1.66 μs, x equals to the gap length between the main electrodes, 3 cm. The value of $t\text{-}t_1$, 240 ns, is very close to the optimum of $t_{G3\text{-}BD}$, 220 ~ 240 ns, in Fig. 2. 3. Therefore it is considered that the efficient and homogeneous electron layer reaches the anode and that the whole of the discharge volume is sufficiently ionized at the optimal value of $t_{G3\text{-}BD}$. Most electrons are consequently distributed throughout the discharge volume, and the transition to the homogeneous glow discharge occurs there at the same time.

On the other hand, if the electrons are produced on the surface of the cathode at intervals of half-period T of the HFCD current in both polarities during the main discharge, the homogeneous electron layers successively propagate across the main electrodes along the electric field. Fig. 2. 12 shows the development of the electron homogeneous layers, represented by "e" from the cathode to the anode at intervals of T like a streak-mode photograph. The value $t_{K\text{-}A}$ represents the time required for the layers to propagate across the main

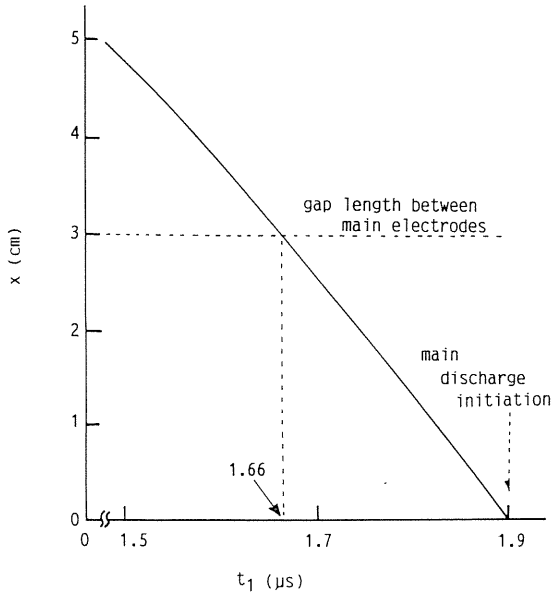

Fig. 2. 11. Relationship between developing distance x and time t_1.

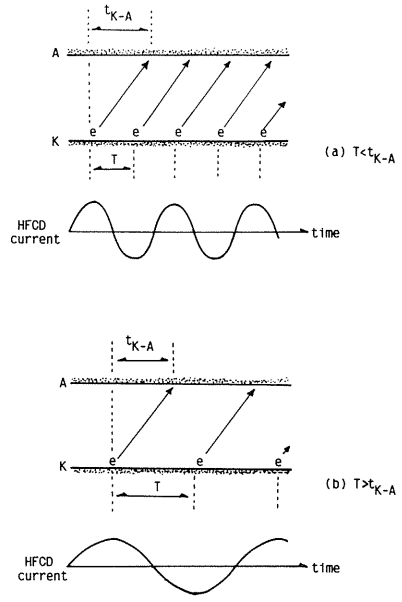

Fig. 2. 12. Schematic successive propagations of homogeneous electron layers at intervals of T (a) for $T > T_{K-A}$ and (b) for $T < T_{K-A}$. The value T_{K-A} represents the time required for the layer to propagate across the main electrodes. The symbol "e" represents a homogeneous electron layer.

electrodes. No homogeneous layer is periodically in the discharge volume for the time of $T\text{-}t_{K\text{-}A}$ in the case of $T > t_{K\text{-}A}$, whereas one homogeneous layer is always there at least in the case of $T \leqq t_{K\text{-}A}$. The homogeneous layers suppress the formation of filamentary streamer and maintain the glow discharge due to the uniformity of the electric field on the layers. The glow-to-arc transition is considered to occur when there are no layers in the discharge volume during the main discharge. Therefore it is important that there is at least one homogeneous layer in the discharge volume to suppress the glow-to-arc transition, and it is necessary to produce the layers frequently on the surface of the cathode.

When E in Eq. (2-1) is the average electric field in the discharge volume for 1 μs after the initiation of the main discharge, it is estimated that the electrons starting from the cathode reach the anode at 300 ns. The shorter the half-period T between first and next layers is down to 300 ns, the larger the laser output becomes as shown in Fig. 2. 9. This results is consistent with the above model.

2. 3. 3. Analysis of HFCD Current using Equivalent Circuit

It is necessary for the waveform of the HFCD current to satisfy the following condition to increase the laser output according to the results of the previous experiments: high peak value (for I_p), short period (for T), long duration (> 1 μs for t_e). Therefore, it is useful to calculate the HFCD current and to suggest the optimal parameters in the HFCD circuit for the increase of the laser output.

The HFCD current is considered to be the transient current for charging C_s and C_g from the charged capacitance C_3, where the following conditions are assumed to simplify the calculations.

1) The impedance of the main discharge circuit, including the discharge volume, is negligible compared with the impedance of C_s.
2) The voltage across the main electrodes is assumed to equal the constant value of the breakdown voltage V_{BD} after the spark of G_3.
3) The impedance of the corona discharge between the cathode and the trigger electrode is given by the constant resistance of R_g.

The equivalent circuit of the HFCD circuit is shown in Fig. 2. 13, where V_{BD} is the breakdown voltage of the main discharge, R_s is the resistance of the electrical line, C_g is the capacitance of the glass tube, L_g is the inductance at the trigger electrode. It is so difficult to resolve the HFCD current analytically that it is computed numerically.

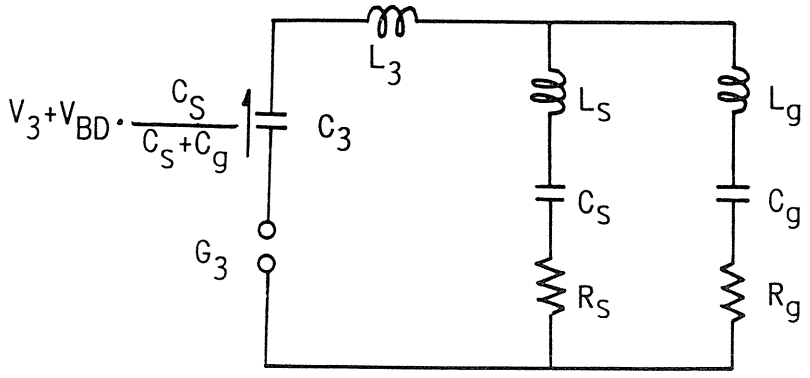

Fig. 2. 13. Equivalent circuit for calculation.

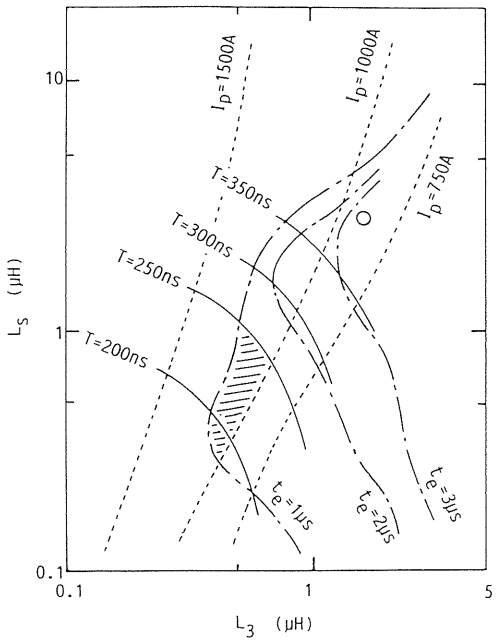

Fig. 2. 14. Calculated contour lines of peak value I_p, half-period T and duration t_e as functions of inductances L_s and L_3. The circle (○) represents the values of L_3 and L_s measuring I_p, T and t_e.

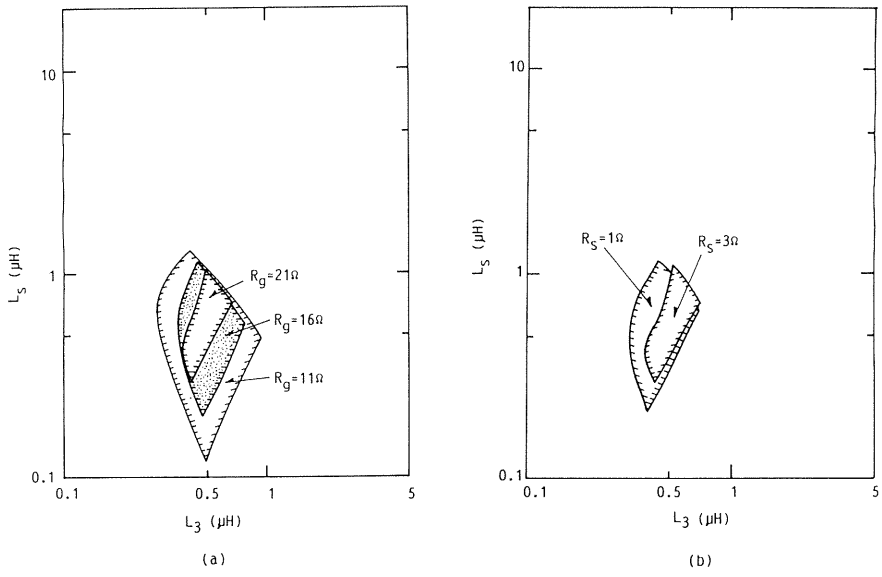

Fig. 2. 15. Calculated region of inductances L_s and L_3 under the condition of $I_p > 1000$ A, $T < 250$ ns, $t_e > 1$ μs as parameters of resistances (a)R_g and (b)R_s.

Figs. 2. 10 shows the calculated values of I_p, T and t_e as a function of C_s. The comparatively good agreement between observed and calculated values is obtained at L_3=1.7 μH, L_s=2.5 μH, L_g=90 nH, R_g=21 Ω and R_s=3 Ω.

Fig. 2. 14 shows the calculated contour lines of I_p, T and t_e as functions of L_s and L_3 at C_s=3400 pF, C_3=40 nF and V_3=20 kV. The duration t_e is very short for $L_s >> L_3$ because of no oscillation due to over-damping, and I_p decreases for $L_s << L_3$ because the HFCD current is more apt to flow into C_s. Therefore there is the optimal relation between L_3 and L_s in the HFCD current flow according to the condition for the increase of the laser output. The measurement of I_p, T and t_e is performed at the values of L_3 and L_s shown by the circle (○) in Fig. 2. 14, because L_3 and L_s are limited to ≧1.7 μH and ≧2.5 μH, respectively, due to the structure of the laser device. If L_3 and L_s can be reduced in accordance with the shaded portion in Fig. 2. 14, the conditions of $I_p > 1$ kA, $T < 250$ ns, $t_e > 1$ μs will be satisfied. Consequently, it is expected that greater laser output would be obtained without the glow-to-arc transition than that in this experiment where the best condition of I_p, T and t_e are obtained at C_s=850 pF as about 800 A, 300 ns and 1.5 μs, respectively. Also, Figs. 2. 15(a) and 2. 15(b) show the part which satisfies the conditions of $I_p > 1$ kA, $T < 250$ ns, $t_e > 1$ μs at R_g=11 Ω, 16 Ω, 21 Ω and at R_s=1 Ω, 3 Ω. It is obvious that the reduction of the resistances R_s and R_g serves to enlarge the area of such condition. Consequently, it may be possible to increase the laser output for the input energy density over 220 J/l in a future study.

3. Development of Corona-Preionized TEA-CO_2 Laser with HFCD Circuit Recycling Residual Energy

3. 1. Experimental Apparatus and Procedure

Fig. 3. 1 shows the electrical circuit of the laser device with the SC-HFCD circuit. The same apparatus as the previous chapter except the SC-HFCD circuit is used. The SC-HFCD circuit enclosed by the broken line is composed of the capacitances C_{31} and C_{32} in the two-stage Marx bank, the collecting capacitance C_{30}, the diode D and the inductance L_d. The inductance L_d restricts the amplitude of the current through the diode D so as not to exceed the permitted value of surge current for the diode. The operating sequence of the SC-HFCD circuit is described in 3. 2 in detail. The waveforms of the voltage across the main electrodes, the main discharge current, the laser power and the current through the trigger electrode are measured in the same way as chapter 2. The waveform of the current through the diode D is measured with a shunt resistor. The voltage V_{C3}, which is the voltage applied on C_{30}, C_{31} and C_{32} before the laser operation, is measured with an electrostatic voltmeter.

3. 2. Operating Sequence of SC-HFCD Circuit

Fig. 3. 2 shows the typical waveforms of (a)the voltage V across the main electrodes, (b)the main discharge current I_m, (c)the laser power, (d)the current through the trigger electrode, I_t, and (e)that through the diode D, I_d, in the steady-state operation described later, where the SC-HFCD circuit has a two-stage Marx bank as shown in Fig. 3. 1. The operating parameters are L_1=10 μH, C_1=C_2=40 nF, C_{30}=75 nF, C_{31}=40 nF, C_{32}=100 nF and V_1=68.1 kV, where V_1 is the voltage applied on C_1. The capacitances C_{30}, C_{31} and C_{32} are charged at the voltages V_{30}, V_{31} and V_{32}, respectively, and these voltages remains at a certain voltage V_{C3} before the laser operation.

After the nitrogen-sealed gap G_1 is triggered, the voltage V is applied across the main electrodes and the trigger current passes through the capacitance C_s before the sparks of the

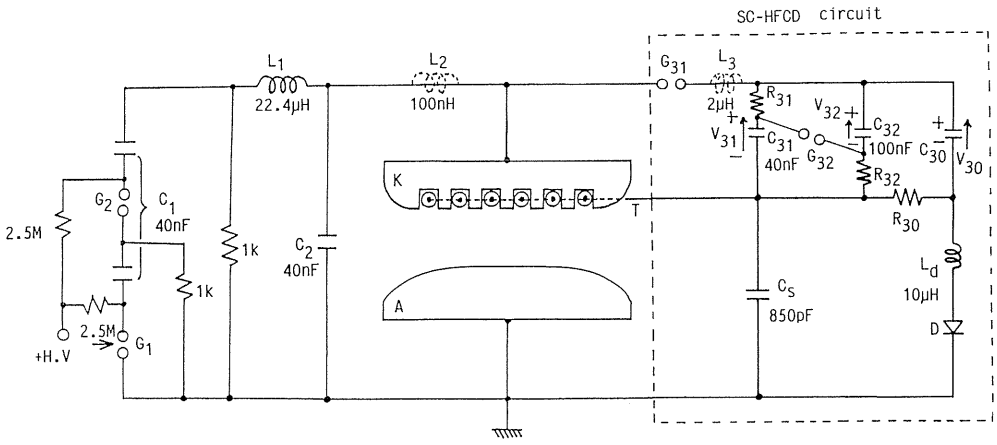

Fig. 3. 1. Schematic diagram of experimental apparatus and electrical circuit.

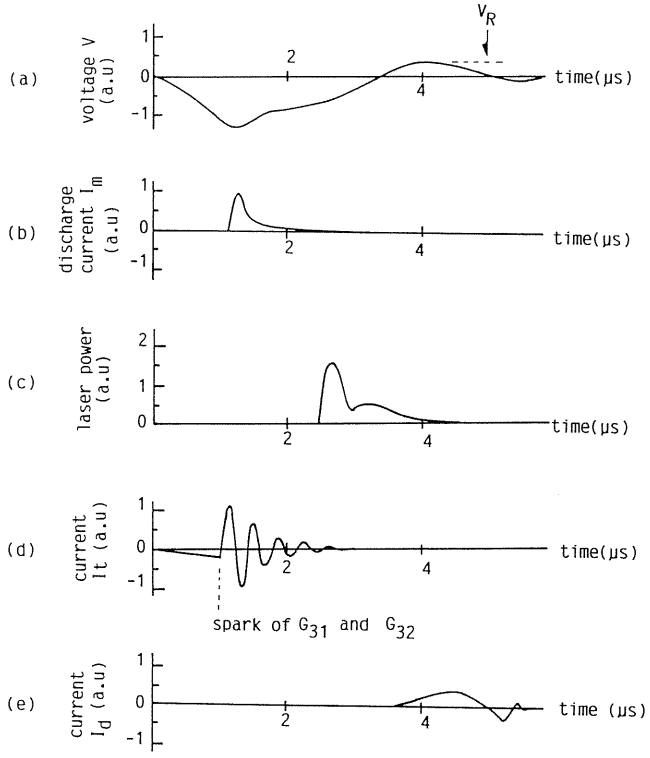

Fig. 3. 2. Temporal characteristics of (a) voltage across the main electrodes, V, (b) main discharge current, I_m, (c) laser power and (d) current on the trigger electrode, I_t, and (e) that on diode D, I_d, with the operation of SC-HFCD circuit.

main electrodes gap and the gaps G_{31} and G_{32}. When V exceeds a critical value, the gaps G_{31} and G_{32} are automatically fired and the output voltage V_{out} of the Marx bank in the SC-HFCD circuit is applied between the trigger electrode and the cathode, where V_{out} is estimated as the value multiplying V_{C3} by the stage number of the Marx bank. The triggering time is controlled by the pressure of the nitrogen gas sealed in G_{31} and G_{32}. Consequently, the HFCD current flows by L-C oscillation through the trigger electrode, C_{31}, C_{32} and L_3. The discharge volume between the main electodes is mainly preionized by the HFCD current prior to the main discharge because the HFCD current has the higher peak value than the trigger current passing through C_s. The flow of the HFCD current also causes V_{31} and V_{32}, the voltages on C_{31} and C_{32}, to drop in proportion to Q_{out} which represents the amount of electrical charge flowing out of the Marx bank in the SC-HFCD circuit.

Before the polarity of V reverses, most of the energy stored on C_1 is injected into the discharge volume and the CO_2 molecules are excited, whereas 5 ~ 10% of the stored energy, E_R, is not injected and remains in the main discharge circuit. Therefore the reverse voltage V_R appears as shown in Fig. 3. 2(a) because of both the increase of the impedance in the main discharge volume and the L-C oscillation in the circuit of C_1-L_1-C_2. The residual energy E_R becomes usually the loss by heating of resistances. In this laser device with the SC-HFCD circuit, a part of E_R is collected and recycled as the energy for the HFCD in the next operation in the following way.

The voltages of V_{30}, V_{31} and V_{32} before the laser operation are equal to V_{C3}. When a glow discharge is produced in the main discharge volume, V is gradually decreased after the main discharge initiation and is increased again up to V_R in the opposite polarity as shown in Fig. 3. 2(a). Consequently, when V_R is larger than V_{C3}, the charging current flows to C_{30} in the circuit of G_{31}-C_{30}-L_d-D with the electromotive force of V_R-V_{C3} due to the application of the forward voltage on the diode D, and the amount of electrical charge, Q_{in}, is supplied to C_{30}. Then the voltage V_{30} is the value higher than V_{C3} because of collecting the residual energy, whereas the voltages V_{31} and V_{32} are the values lower than V_{C3} because of passing the HFCD current. After the recovery of the insulation in the gaps G_{31} and G_{32}, C_{31} and C_{32} in the Marx bank are slowly charged from C_{30} through the several mega-ohm resistances R_{30}, R_{31} and R_{32}. The voltages V_{30}, V_{31} and V_{32} accordingly settle at a certain value V_{C3}' lower than V_R. If the amount of electrical charge consumed for the HFCD operation is equal to that supplied to C_{30} from PFN while the reverse voltage appears, V_{C3}' is equal to V_{C3}. Then the voltages V_{30}, V_{31} and V_{32} can be maintained at V_{C3} between shots, and the successive laser operation is possible without the change of V_{30}, V_{31} and V_{32}. It is called as the steady-state operation. Thus the residual energy collected in C_{30} is distributed to C_{31} and C_{32}, and is recycled as the energy for the HFCD in the next laser operation.

When V_1 is a relatively large value, a glow discharge is not produced in the first laser operation where V_{30}, V_{31} and V_{32} are zero, because the main discharge volume is preionized only by the trigger current through C_s. However, when V_1 is a relatively low value, a glow discharge is produced even without the HFCD operation, and C_{30}, C_{31} and C_{32} are charged if the reverse voltage V_R appears. Then it is possible to superpose the HFCD on the main discharge because C_{31} and C_{32} are charged, and a glow discharge is produced evenwhen V_1 is increased slightly. As the reverse voltage V_R is increased with V_1 as described in 3. 3. 1, V_{30}, V_{31} and V_{32} are increased and a glow discharge is maintained even at the higher V_1. Therefore, repeating such a procedure, the steady-state operation is obtained even at a relatively high voltage of V_1.

3. 3. *Experimental Results*

3. 3. 1. *Determination of PFN Parameters and Laser Mixture Gas for SC-HFCD Circuit*

Under the condition that the reverse voltage V_R is so small, the SC-HFCD circuit can not be operated because it is difficult to collect the residual energy due to the small electromotive force in the circuit of G_{31}-C_3-L_d-D. Therefore, it is necessary to determine the conditions of the PFN parameters and the laser mixture gas so as to enlarge V_R without the decrease of the laser output.

The following parameters are determined in the laser device without the SC-HFCD circuit.

(1) PFN parameters of C_1, C_2 and L_1

Sato et al.[24] has reported that the ratio C_2/C_1 of about one and C_1 over 20 nF are preferable to obtain large laser output. Therefore, the combinations (C_1,C_2) of (40 nF,40 nF) and (60 nF,52 nF) as well as L_1 between 1 μH and 22.4 μH are examined in this experiment.

(2) Ratio of N_2, CO_2 and He in the laser mixture gas

As shown in Fig. 3. 3, the optimal ratio of N_2/CO_2 in the laser mixture gas is 1:1, and this mixture ratio has been popularly used[25)-28)]. Therefore the optimal ratio of He is examined at atmospheric pressure, changing the flow rate of He to other gases at a constant flow rate of N_2/CO_2=1/1(l/min).

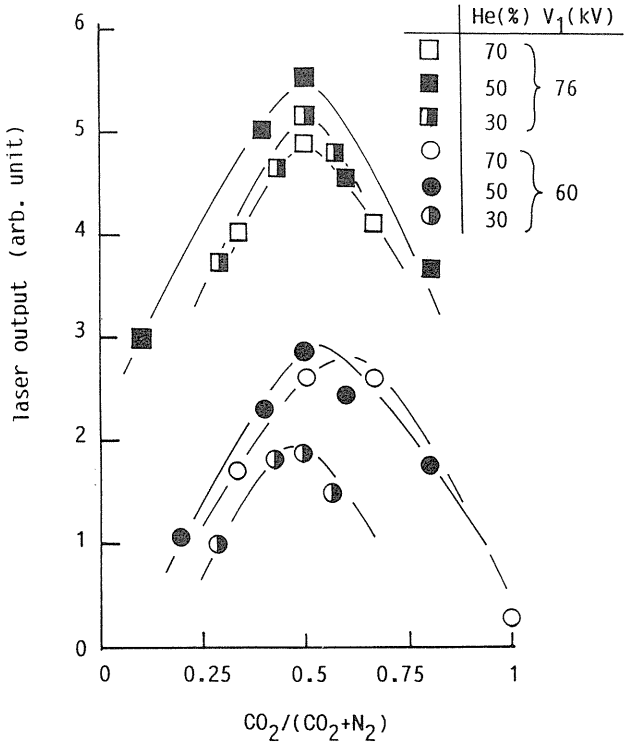

Fig. 3. 3. Variation of laser output as a function of CO_2/N_2 mixture ratio as parameters of voltage V_1 and mixture ratio of He.

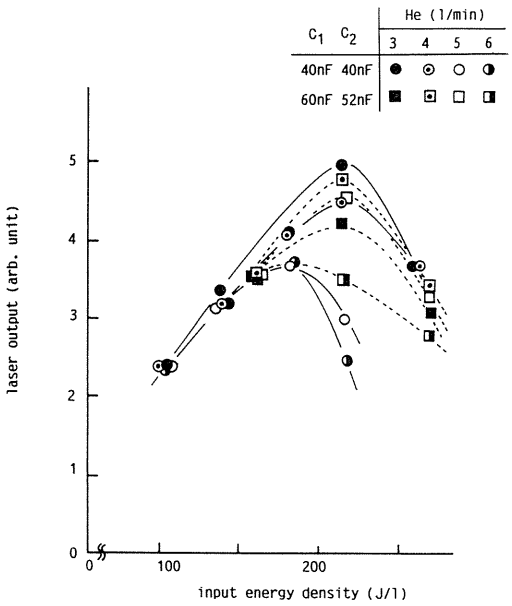

Fig. 3. 4. Relationship between input energy density and laser output as parameters of flow rate of He and combination (C_1,C_2) at L_1=10 μH.

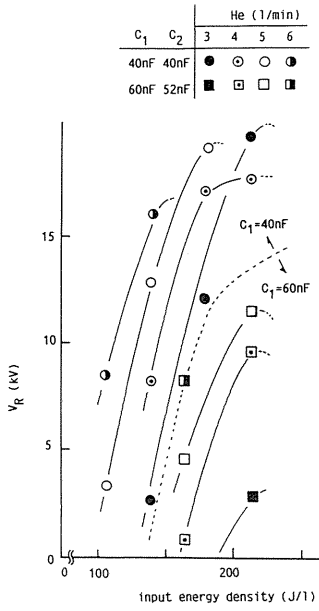

Fig. 3. 5. Variation of reverse voltage V_R with input energy density as parameters of combination (C_1,C_2) and flow rate of He at L_1=10 μH.

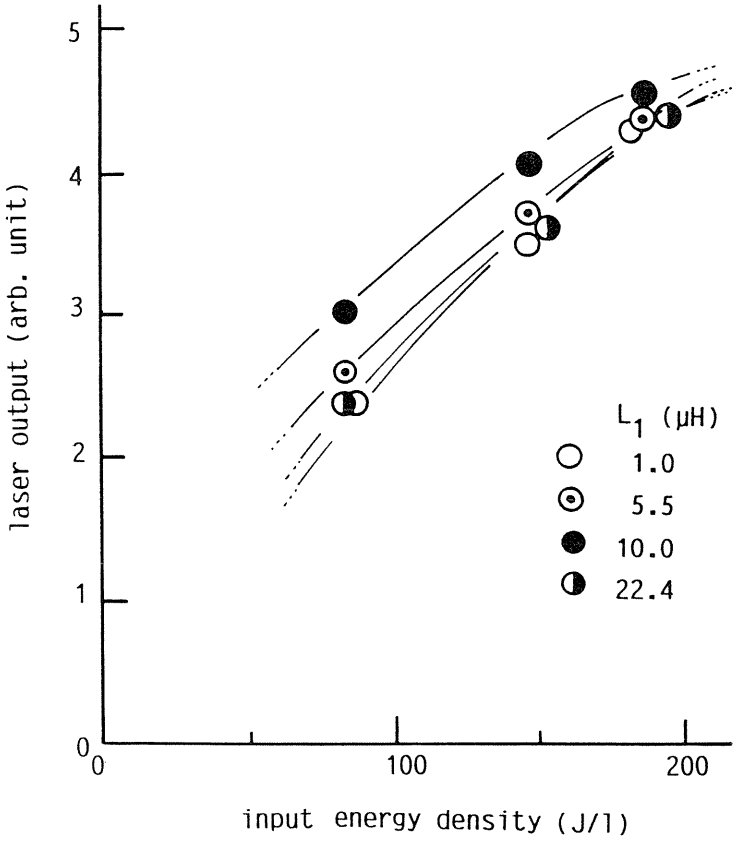

Fig. 3. 6. Variation of laser output with input energy density as a parameter of L_1.

Fig. 3. 4 shows the relationship between the input energy density and the laser output as parameters of (C_1,C_2) and the flow rate of He at L_1=10 μH. When the flow rate of He is 3(l/min) at (C_1,C_2)=(40 nF,40 nF) or 4(l/min) at (C_1,C_2)=(60 nF,52 nF), the laser output has a maximum value at the input energy density of 220 J/l.

Fig. 3. 5 shows the variation of the reverse voltage V_R with the input energy density as parameters of (C_1,C_2) and the flow rate of He. The voltage V_R at (C_1,C_2)=(40 nF,40 nF) becomes so large as compared with that at (C_1,C_2)=(60 nF,52 nF). On the other hand, V_R is increased with the input energy density. This characteristic of V_R is favorable to the suppression of the glow-to-arc transition as described in 3. 3. 3.

Fig. 3. 6 shows the variation of the laser output with the input energy density up to 200 J/l as a parameter of L_1, where (C_1,C_2) is (40 nF,40 nF). The laser output is increased with L_1 up to 10 μH, whereas the glow-to-arc transition described in the previous chapter causes the laser output to decrease for $L_1 > 10$ μH. A similar tendency has been reported by Sato et al.[24].

According to the above results, (C_1,C_2), L_1 and the flow rate of He are determined to be (40 nF,40 nF), 10 μH and 3(l/min), respectively, as the suitable condition to enlarge V_R without the decrease of laser output.

3. 3. 2. Improvement of Laser Output with SC-HFCD Circuit

Fig. 3. 7 shows the relationship between the input energy density and the laser output in the steady-state operation at C_{30}=75 nF as a parameter of the stage number of the Marx bank in the SC-HFCD circuit. When the stage number is equal to 1, the SC-HFCD circuit is operated both with the shortening of R_{31} and without the spark of G_{32}. The laser output without the SC-HFCD circuit is saturated at the input energy density of 230 J/l because of the occurrence of the glow-to-arc transition, while the laser output with the SC-HFCD circuit is increased for the input energy density over 230 J/l. Using the SC-HFCD circuit with a two-stage Marx bank, the maximum laser output of 8.75 J is obtained at the input energy density of 250 J/l, and the arc-free condition is maintained for the input energy density up to 230 J/l. The laser output of 8.75 J corresponds to the output energy density of 17.5 J/l. It is suggested from these results that the SC-HFCD circuit with a multi-stage Marx bank is effective for the increase of the laser output due to the suppression of the glow-to-arc transition.

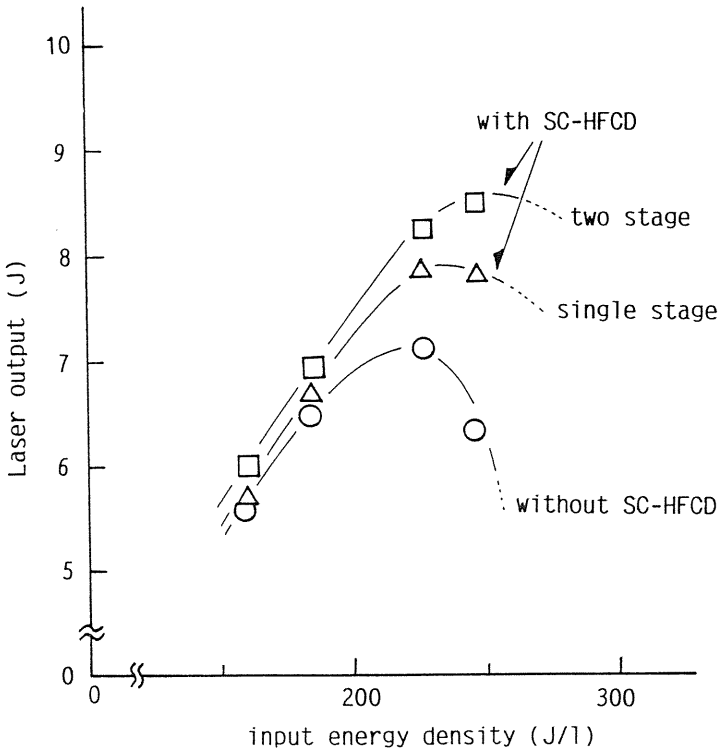

Fig. 3. 7. Relationship between input energy density and laser output as a parameter of stage number of Marx bank in SC-HFCD circuit.

3. 3. 3. Characteristics of Output Voltage V_{out} of SC-HFCD Circuit

It is useful to examine the characteristics of the output voltage V_{out} of the Marx bank in the SC-HFCD circuit because V_{out} have much influence on the HFCD operation, the laser output and the stability of the main discharge.

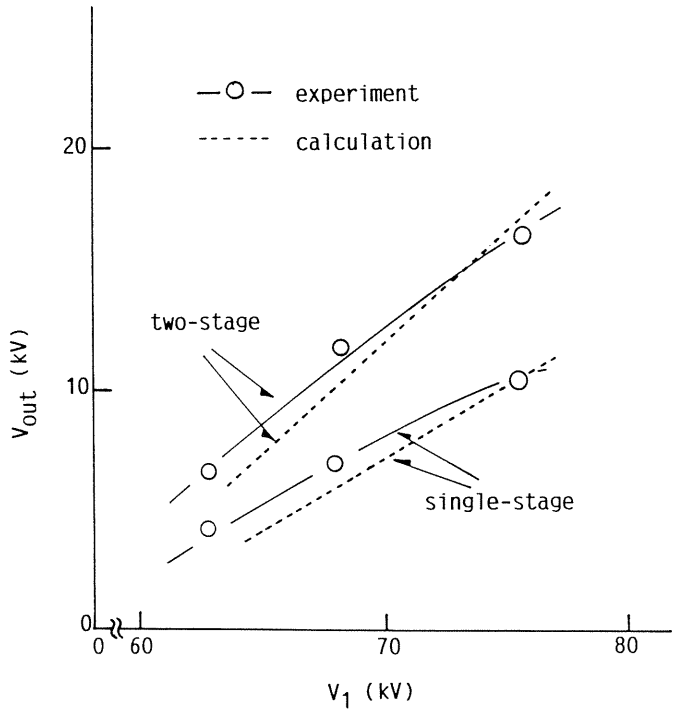

Fig. 3. 8. Dependence of output voltage V_{out} on applied voltage V_1 as a parameter of stage number of Marx bank in SC-HFCD circuit.

Fig. 3. 8 shows the relationship between V_{out} and the voltage V_1 applied on C_1 in the steady-state operation at C_{30}=75 nF as a parameter of the stage number of the Marx bank in the SC-HFCD circuit, where V_1 of 68.1 kV corresponds to the input energy density of about 186 J/l. The voltage V_{out} with a two-stage Marx bank is larger than that with a single-stage one, and the laser output is increased with the stage number as shown in Fig. 3. 7. On the other hand, V_{out} is increased with V_1 because of the increase of the reverse voltage V_R. This tendency in V_{out} is favorable to suppress the glow-to-arc transition, because it is necessary for the HFCD current to have a higher peak value as the input energy density is increased. The characteristics of V_{out} are discussed in 3. 6, using the equivalent circuit.

After the charging current flows into C_{30} through the diode D, the recovery current of the diode is observed in the polarity opposite to the charging current as shown in Fig. 3. 2(e). As the amount of electrical charge due to the recovery current is not so small, it causes V_{out} to be reduced. Therefore the voltage V_{out} will be larger if the diode D has a good recovery ability.

3. 3. 4. Decrease of Output Voltage V_{out} with Occurrence of Glow-to-Arc Transition

When the glow-to-arc transition occurs, the capacitance C_{30} cannot be charged and the voltage V_{out} is decreased because of the rapid reduction of the reverse voltage. It is important to make the decrease of V_{out} due to the glow-to-arc transition as small as possible so as to insure the laser operation even if the glow-to-arc transition should occur.

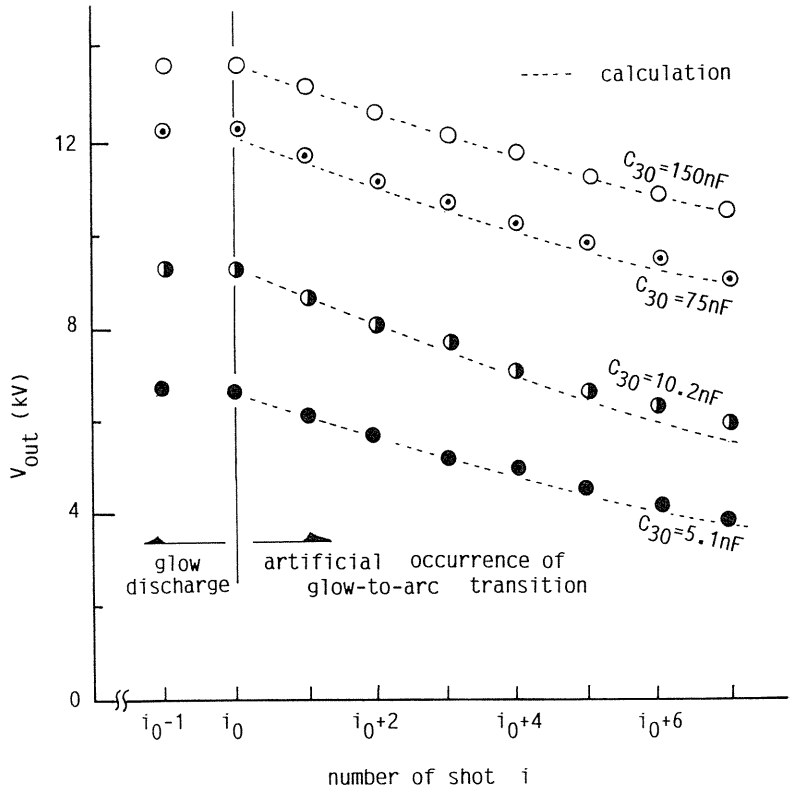

Fig. 3. 9. Decrease of output voltage V_{out} due to glow-to-arc transition with number of shot, i, as a parameter of C_{30}.

Fig. 3. 9 shows the decrease of V_{out} due to the glow-to-arc transition with the number of shot, i, as a parameter of C_{30}, where V_1 is 68.1 kV and the control of triggering time of the HFCD current due to the change of the gas pressure in G_{31} makes the glow-to-arc transition rate be 100% artificially after C_{30}, C_{31} and C_{32} are sufficiently charged in the steady-state operation until i_0 using the SC-HFCD circuit. The voltage V_{out} is gradually decreased with i, and is maintained at a relatively high value with the increase of C_{30} even if the several glow-to-arc transitions occur successively. Therefore it is required to increase C_{30} in order to insure the laser operation against the glow-to-arc transition because the keep of V_{out} at a high value leads to the suppression of the glow-to-arc transition.

3. 4. Calculation of the Output Voltage of the SC-HFCD Circuit

As described in 2. 4. 3, the HFCD current is considered to be the transient charging current from the Marx bank in the SC-HFCD circuit to the parallel-connected capacitances C_s and C_g (the capacitance of the glass tubes which cover the trigger electrodes) under the condition that the impedances of the PFN and the main discharge plasma are negligible compared with C_s. The output voltage V_{out} of the SC-HFCD circuit is here calculated and compared with the experimental results.

Assuming that V_{C3}, which is equal to the voltages on C_{30}, C_{31} and C_{32} before the laser operation, changes to V_{C3}' after the laser operation, V_{C3}' is related with V_{C3} by the following equation on the charge conservation:

$$\sum_{i=0}^{n} C_{3i} \cdot V_{C3}' = \sum_{i=0}^{n} C_{3i} \cdot V_{C3} - n \cdot Q_{out}(V_{C3}) + Q_{in}(V_1, V_{C3}) , \tag{3-1}$$

$$V_{out} = n \cdot V_{C3} , \tag{3-2}$$

where n is the stage number of the Marx bank in the SC-HFCD circuit (n=1 or 2 in this experiment), C_{3i} at i=0 is the electrostatic capacity of the capacitance C_{30} to collect the residual energy and C_{3i} for $i \geqq 1$ is that of i-th stage capacitance in the Marx bank. The value Q_{in} is the amount of electrical charge supplied to C_{30} while the reverse voltage appears, and the value Q_{out} is that flowing out of each capacitance in the Marx bank by the HFCD current. The value Q_{in} is considered as functions of V_1 and V_{C3}, and it is obvious from the other experimental results shown in Fig. 3. 10 that Q_{in} is decreased linearly with the increase of V_{C3}.

It is assumed that the conductivity of G_{31} and G_{32} is sufficiently maintained until the voltage across the main electrodes disappears. The amount of electrical charge Q_{out} can be approximately expressed by the following equation as a function of V_{C3}, estimating the

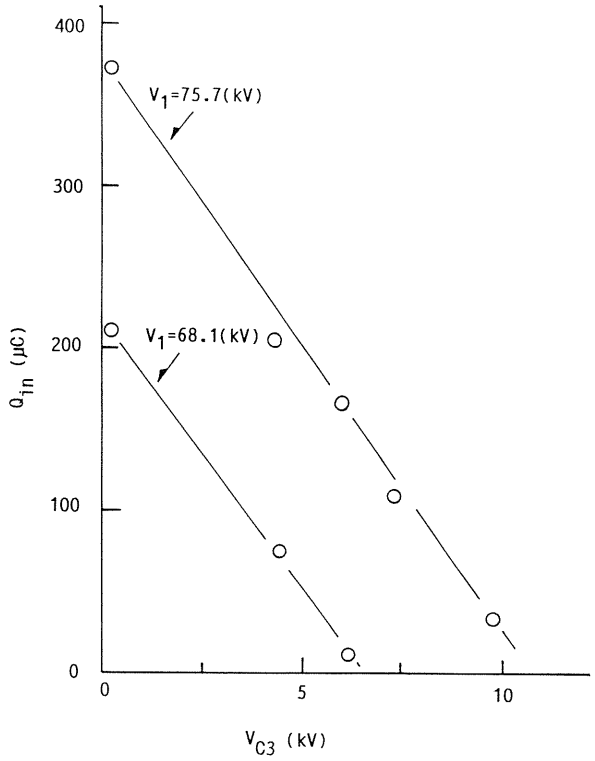

Fig. 3. 10. Relationship between voltage V_{C3} and amount of electrical charge Q_{in} as a parameter of applied voltage V_1.

amount of electrical charge flowing from the series-connected capacitances in the Marx bank, which correspond to C_3 charged at the voltage $n \cdot V_{C3}$ in Fig. 2. 13, to the parallel-connected capacitances of C_s and C_g (the capacitance of the glass tubes which cover the trigger electrodes):

$$Q_{out}(V_{C3}) = \frac{n \cdot V_{C3} \cdot (C_s + C_g) \cdot (1/\sum_{i=1}^{n}(1/C_{3i}))}{C_s + C_g + 1/\sum_{i=1}^{n}(1/C_{3i})}, \tag{3-3}$$

In the steady-state operation, Eq. (3-1) can be transformed to the following equation because V_{C3}' equals to V_{C3}:

$$Q_{in}(V_{C3}) = n \cdot Q_{out}(V_{C3}) . \tag{3-4}$$

Resolving Eq. (3-4) for V_{C3}, the calculated variation of V_{out} expressed by Eq. (3-2) in the steady-state operation is shown in Fig. 3. 8 with the observed value. It is obvious that the comparatively good agreement between the observed and calculated values is obtained.

On the other hand, the decrease of V_{out} due to the glow-to-arc transition is calculated, where the residual energy is not collected because the reverse voltage V_R do not appear. Therefore Eq. (3-2) can be transformed to the following equation, substituting zero and Eq. (3-3) for Q_{in} and Q_{out}, respectively:

$$V_{C3}' = V_{C3} \cdot \left[1 - \frac{n^2 \cdot (C_s + C_g) \cdot 1/\sum_{i=1}^{n}(1/C_{3i})}{(C_s + C_g + 1/\sum_{i=1}^{n}(1/C_{3i})) \cdot \sum_{i=0}^{n} C_{3i}} \right], \tag{3-5}$$

Letting the successive occurrence times of the glow-to-arc transition be m, V_{C3}' can be expressed by the following geometrical progression:

$$V_{C3} = V_{C30} \cdot \left[1 - \frac{n^2 \cdot (C_s + C_g) \cdot 1/\sum_{i=1}^{n}(1/C_{3i})}{(C_s + C_g + 1/\sum_{i=1}^{n}(1/C_{3i})) \cdot \sum_{i=0}^{n} C_{3i}} \right]^{m-1}, \tag{3-6}$$

where V_{C30} is the initial value of V_{C3}. Substituting Eq. (3-6) for Eq. (3-2), the calculated variation of V_{out} at n=2 is shown with broken lines in Fig. 3. 9. The considerably good agreement between the observed and calculated values is obviously obtained. From the above results, the characteristics of V_{out} can be predicted if Q_{in} and the initial value V_{C30} are known.

Next, the energy saved by the SC-HFCD circuit is estimated. If the capacitances in the n-stage Marx bank are charged with another transformer, the energy E_{HFCD} supplied for one HFCD operation is expressed by the following equation:

$$E_{HFCD} = 2 \cdot \left[\sum_{i=1}^{n} \frac{{V_{C3}}^2 \cdot C_{3i}}{2} - \frac{{Q_{out}}^2}{2(C_s + C_g)} - \sum_{i=1}^{n} \frac{(V_{C3} \cdot C_{3i} - Q_{out})^2}{2C_{3i}} \right]. \tag{3-7}$$

In practice, the hysterisis loss and the iron loss in the transformer are added to E_{HFCD}. Eliminating V_{C3} and Q_{out} in Eq. (3-7) by Eq. (3-2) and (3-3), the relation between E_{HFCD} and V_{out} is shown in Fig. 3. 11, where n=2. At V_1=75.8 kV where V_{out} is about 16 kV as shown in

Fig. 3. 8, the energy E_{HFCD} is 0.7 J, while the energy stored on C_1 is about 115 J. Therefore it is estimated that the electric energy is saved by the order of 1 percent of the stored energy using the SC-HFCD circuit.

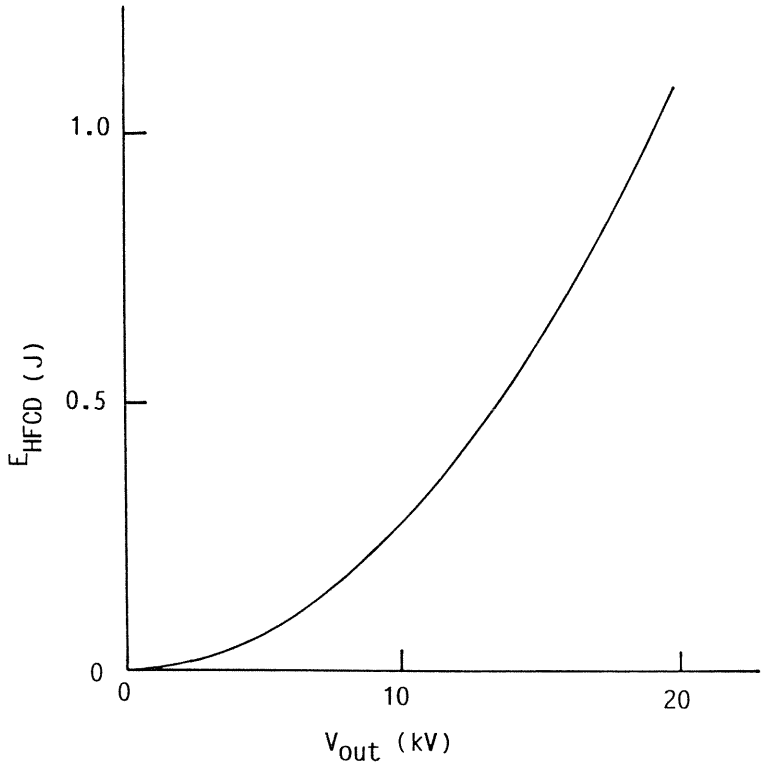

Fig. 3. 11. Relationship between output voltage V_{out} and energy for a HFCD operation, E_{HFCD}.

Although the energy is saved by only ~1% with the SC-HFCD circuit in this experiment, the more energy might be saved when the capacitance of the glass tube or the stage number of the Marx bank is increased to intensify the corona preionization.

4. Generation of Acoustic Vibration in Electric Suspension Insulator with Irradiation of Pulsed CO_2 Laser Beam

4. 1. Experimental Apparatus and Procedure

Fig. 4. 1 shows the schematic diagram of the experimental apparatus. A pulsed laser beam from a TEA-CO_2 laser, focused by a convex germanium lens whose focal length is about 10 cm, is irradiated onto the surface of an electric suspension insulator without a crack. The insulator is made of ceramics with the diameter of about 26 cm. The irradiation intensity

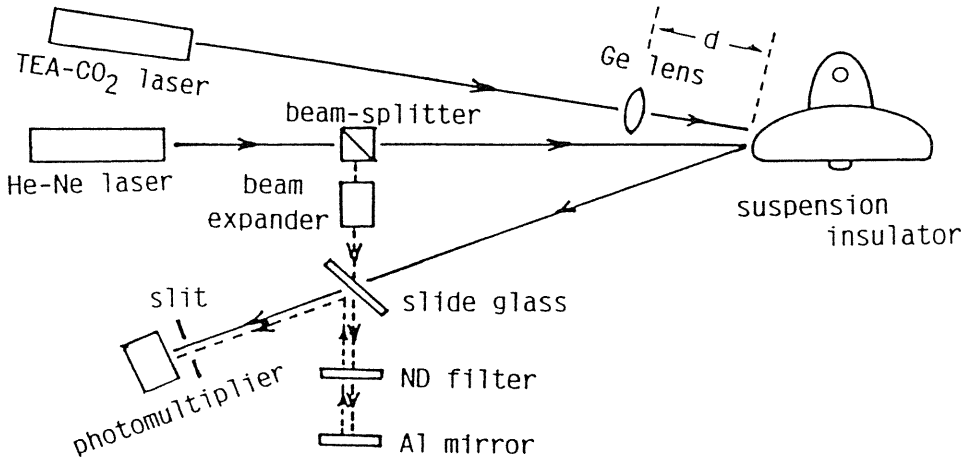

Fig. 4. 1. Schematic diagram of experimental apparatus.

on the surface of the insulator varies both with the laser beam energy in the range of 2.4 ~ 5.9 joules and with the distance between the convex germanium lens and the surface of the insulator, d, as shown in Fig. 4. 1. The diameter and the pulse width of the CO_2 laser beam are about 3 cm and 400 nsec, respectively.

The vibration of the insulator is measured both with a He-Ne laser interferometer and with an acceleration sensor touched on the surface of the insulator. The He-Ne laser beam is divided to two beams by a beam splitter. One beam is irradiated and reflected on the surface of the insulator, and is used through the slide glass as an objective beam of the laser interferometer. Another beam as a reference beam is reflected on the slide glass after passing through the beam expander and the ND filter so that the divergence and the intensity of the reference beam could correspond to those of the objective beam. Overlapping with the objective beam, the reflected reference beam propagates to a photomultiplier through a slit to detect the change of the interference pattern due to the vibration of the insulator. The acceleration sensor has the minimum measurable acceleration of about 10 G and the upper-limit frequency of about 15 kHz, while the laser interferometer has the minimum measurable displacement of about 10 nm and the upper-limit frequency of about 10 kHz.

The amplified signals of the photomultiplier and the acceleration sensor are recorded with the storage oscilloscope so as to analyze the frequency components of the signals by performing Fast Fourier Transform (known as FFT).

4. 2. Experimental Results

4. 2. 1. Phenomena on Surface of Electric Insulator with Irradiation of Laser Beam

Fig. 4. 2 shows the time-integrated photographs of the phenomena on the surface of the insulator irradiated with the CO_2 laser beam as a parameter of d in the range of 3.5 ~ 10.5 cm, where the laser beam energy is about 3 joules. Immediately after the irradiation, the surface slightly shines at d=3.5 cm as shown in Fig. 4. 2(a). However, the increase of d results in heating the surface more locally and strongly, and the plasma spouts from the whole of the spot area at d=8.2 cm as shown in Fig. 4. 2(b). The intensive air breakdown plasma is

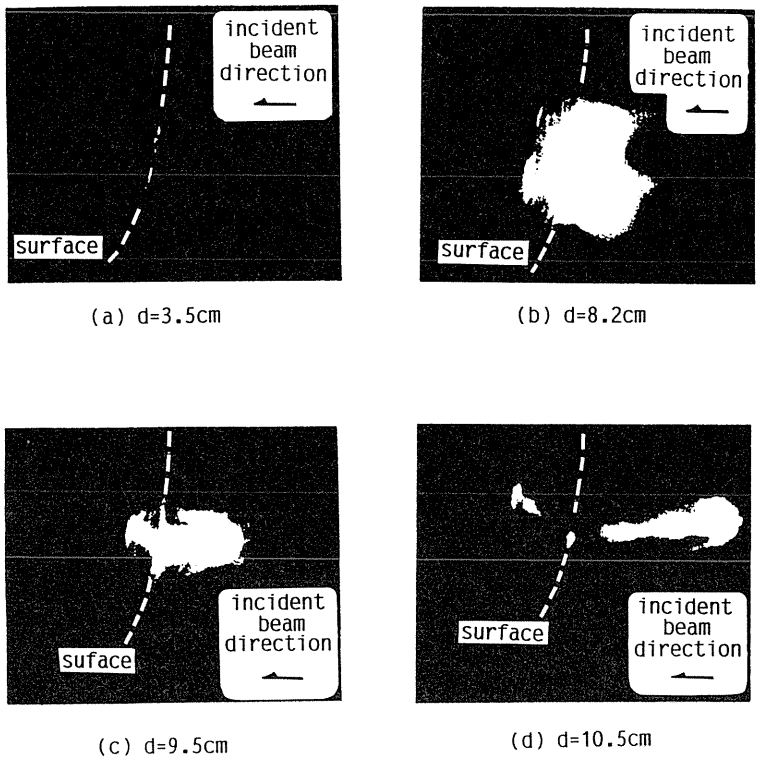

Fig. 4. 2. Phenomena on surface of insulator (a) at d=3.5 cm, (b) at d=8.2 cm, (c) d=9.5 cm and (d) d=10.5 cm.

observed besides the spouting plasma at d=9.5 cm as shown in Fig. 4. 2(c). Furthermore, in the case of d=10.5 cm, the air breakdown plasma can be more clearly observed whereas the spouting plasma is seldom observed as shown in Fig. 4. 2(d), where the focal point of the germanium lens is in front of the surface of the insulator.

The air in front of the insulator is weakly ionized by the strong UV radiation from the spot area with the intensive irradiation of the pulsed laser beam, and the explosive increase of the electrons in the low-ionized plasma due to inverse bremsstrahlung results in the air breakdown.

4. 2. 2. Temporal Variation of Laser-Induced Acoustic Vibration of Electric Suspension Insulator

Fig. 4. 3 shows the temporal waveforms of the signals of the acceleration sensor and the photomultiplier for the electric suspension insulator at d=8.2 cm and 5.9 J of the laser beam energy. These signals continues for more than 100 msec at several kiro-hertz after the irradiation of the laser beam.

Fig. 4. 4 shows the relative temporal variations of the frequency spectrums for the signals of the acceleration sensor and the photomultiplier during the time of 1—31 msec, 70—100 msec, 150—180 msec, 230—260 msec after the irradiation of the laser beam. These

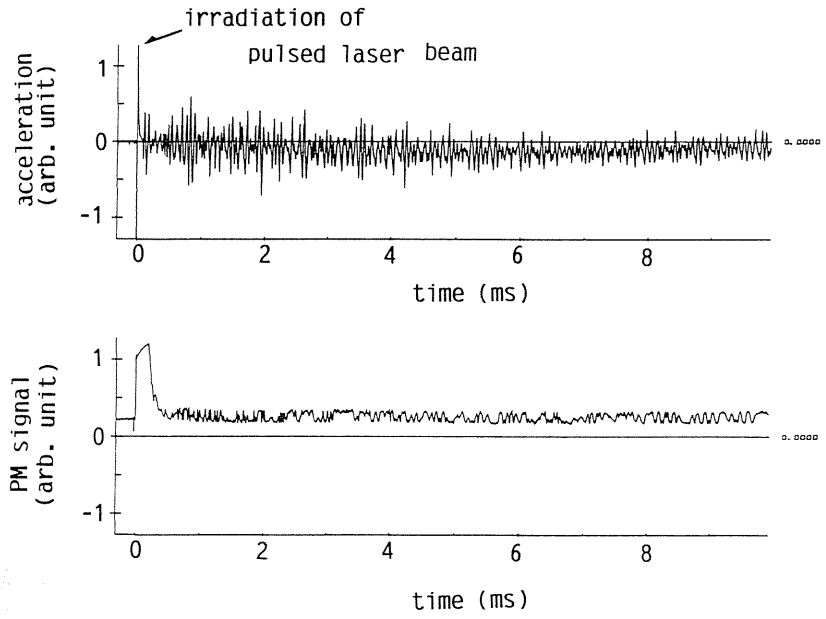

Fig. 4. 3. Transient waveforms of signals of acceleration sensor and photomultiplier.

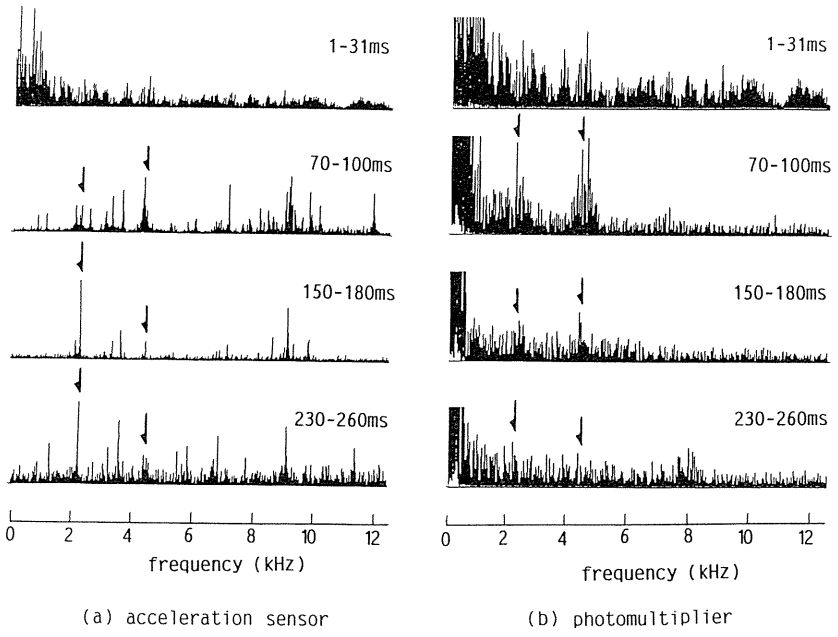

Fig. 4. 4. Temporal relative variations of frequency spectrums for signals of (a) acceleration sensor and (b) photomultiplier.

signals obviously includes many frequency components during 1—31 msec. However, it is found that the insulator continues to be vibrated in a natural mode to depend on the material and the shape of the insulator with the passing of time after 70 msec. The frequency components of 2.2 kHz and 4.4 kHz are more clearly observed in the spectrum of the photomultiplier, comparing with the spectrum of the acceleration sensor. After 230 msec, the natural vibration decays to a degree of the amplitude less than the detectable limitation of the laser interferometer.

4. 2. 3. *Influence of Irradiation Intensity of Laser Beam on Acoustic Vibration of Electric Suspension Insulator*

As shown in Fig. 4. 2, it is observed that the phenomena on the surface of the insulator varies with the distance d between the germanium lens and the surface of the insulator. The dependence of the acoustic vibration on the distance d and the irradiation intensity of laser beam is examined here.

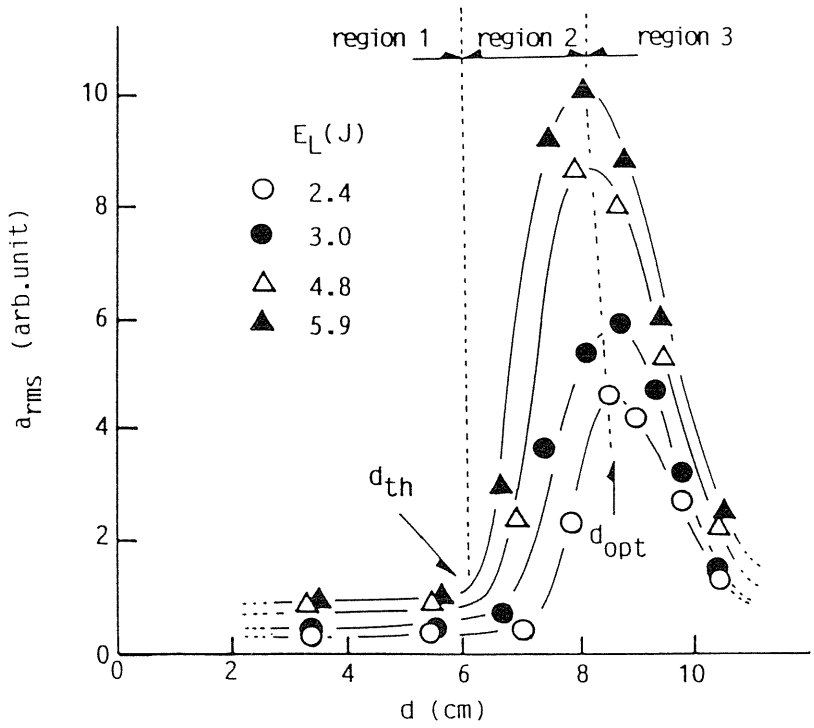

Fig. 4. 5. Variation of acceleration a_{rms} with distance d as a parameter of laser beam energy E_L.

Fig. 4. 5 shows the variation of a_{rms} with d as a parameter of the laser beam energy E_L, where a_{rms} is defined as the root mean square value of the acceleration for 2 ms after the irradiation of the laser beam and indicates the amplitude of vibration in the insulator. The acceleration a_{rms} shows the maximum value at $d=d_{opt}$(8 ~ 9 cm), and the variation of a_{rms} consists of the following three regions.

1) region 1: the acceleration a_{rms} is independent of d for $d < d_{th}$.
2) region 2: the acceleration a_{rms} is increased with d for $d_{th} < d < d_{opt}$.
3) region 3: the acceleration a_{rms} is decreased with d for $d > d_{opt}$.

The phenomena on the surface of the insulator in the regions 1, 2 and 3 correspond to the photographs of Fig. 4. 2(a), (b) and (c), respectively.

Fig. 4. 6 shows the relationship between a_{rms} and the irradiation intensity on the surface of the insulator rearranging the results shown in Fig. 4. 5. The amplitude of a_{rms} is rapidly increased correspondingly to the spout of plasma from the surface for the irradiation intensity over about 2×10^7 W/cm^2, whereas the amplitude is decreased correspondingly to the generation of the air breakdown plasma in front of the surface of the insulator for the irradiation intensity over about 6.5×10^7 W/cm^2.

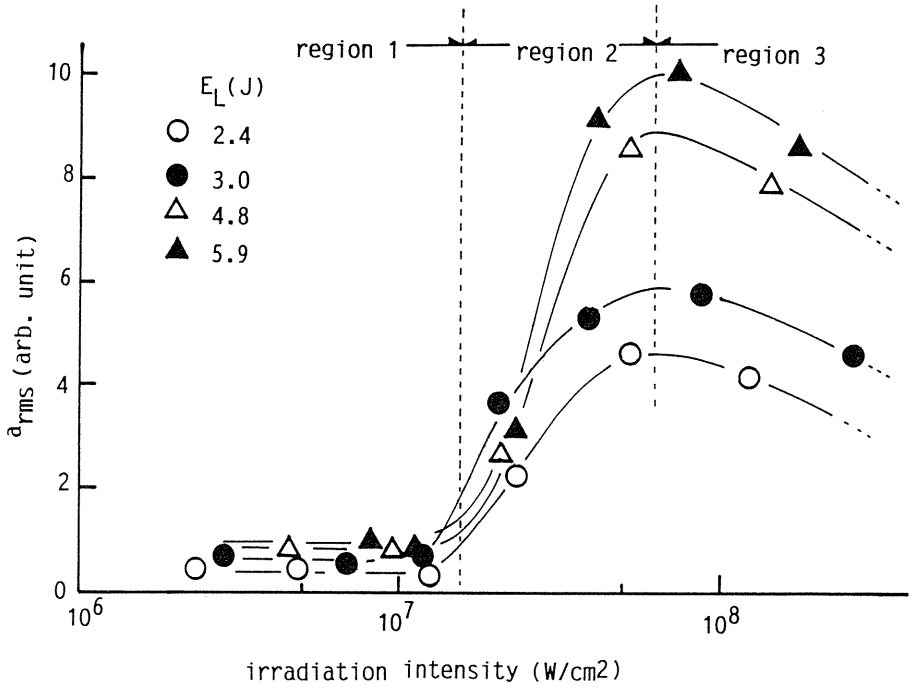

Fig. 4. 6. Variation of acceleration a_{rms} with irradiation intensity of laser beam as a parameter of laser beam energy E_L.

4. 3. Excitation Mechanism of Natural Vibration with Laser Irradiation

The acceleration a_{rms} intensively depends on the irradiation intensity and the phenomena on the surface of the insulator as described in 4. 2. 3. It is suggested that the observed plasma and the generated heat on the surface are associated with the vibration of the insulator, and the following processes are considered as the principles of the vibration; 1)the thermal shock by heating of the laser beam, 2)the reaction of the particles spouting from the insulator, 3)the shock wave from the air breakdown plasma generated by the laser beam in front of the surface of the insulator. In this section, the principle of the vibration in each region shown in

Figs. 4. 5 and 4. 6 is investigated on the basis of the time-integrated photographs shown in Fig. 4. 2, and the observed characteristics of a_{rms} are relatively compared with the calculated forces F_1, F_2 and F_3 applied on the surface of the insulator in each region. The surface of the insulator is assumed to be an infinite plane to simplify the calculation.

(1) Deduction of force F_1 in region 1

It is considered that the thermal shock is a dominant vibration force because the laser-produced plasma is seldom observed on the surface in this region. The maximum of the stress applied on the surface of the insulator, σ_{max}, is expressed by the following equation under the condition of the free surface according to the paper reported by Gournay[29]:

$$\sigma_{max} = \frac{v\beta M}{2\rho C} I_0 , \tag{4-1}$$

where v is the velocity of thermal-wave propagation, β is the coefficient of linear thermal expansion, M is the molecular weight, ρ is the density, C is the specific heat per mole and I_0 is the irradiation intensity on the surface. The irradiation intensity I_0 and the wave velocity v are expressed by the equations, $I_0=E_L/\tau S$ and $v=(\varepsilon/\rho)^{1/2}$, respectively, where E_L is the laser beam energy, τ is the pulse duration of the laser beam, S is the irradiated area and ε is the modulus of elasticity. Multiplying σ_{max} by S, the force F_1 applied on the surface in the region 1 is expressed by

$$F_1 = \sigma_{max} \cdot S = \frac{\beta M \varepsilon^{1/2} E_L}{2 C \rho^{3/2} \tau} . \tag{4-2}$$

(2) Deduction of force F_2 in region 2

It is considered that the reaction of the particles spouting from the surface of the insulator is a dominant vibration force because of the observation of the intensive plasma spouting from the spot area in this region. However it is necessary to consider the transform of the laser beam energy not only to accelerate the spouting particles but also to change the phase of the surface material of the insulator, i.e. melting and vaporizing. According to the paper reported by Shimomura et al.[30], most of the irradiated beam energy is transformed into the kinetic energy of charged or neutral particles, while about 10% of the beam energy is reflected on the surface of a metal target. Other following processes can be neglected as compared with the conversion to the kinetic energy; the radiation from a spouting plasma, the ionization of the metal vapor, the thermal conduction in the metal target and so on. However, the reflection on the insulator can be neglected in this experiment because the insulator is made of porcelain which absorbs the far-infrared radiation so much. Therefore, only the kinetic energy of the spouting particles and the energy required to change the phase of material in the spot area on the insulator are considered, and it is assumed that the whole laser beam energy is absorbed on the surface of the insulator.

The following equation expresses E_t, the energy used to change from a solid phase to a gas phase, using 1 which is the thermal diffusion length of the insulator:

$$E_t = \frac{(f-d)^2 S_0 l \rho}{M f^2} [C(\Delta T_{m-r} + \Delta T_{b-m}) + C_m] + \frac{m}{M} C_b , \tag{4-3}$$

$$1 = (4 MK\tau/\rho C)^{1/2} ,$$

where f is the focal length of the germanium lens, d is the distance between the germanium lens and the surface of the insulator, S_0 is the area of the laser beam before the incidence into the germanium lens, $\Delta T_{m\text{-}r}$ is the temperature difference between the room temperature and the melting point of the insulator, $\Delta T_{b\text{-}m}$ is the temperature difference between the melting point and the boiling point of the insulator, C_m and C_b are the latent heat of fusion and evaporization, respectively, K is the heat conductivity and ρ, C, M, τ are described in Eqs. (4-1) and (4-2).

The acceleration of the insulator, a, is expressed by[31)]

$$a = \frac{2}{u \cdot m_0} \cdot \frac{dE_a}{dt}, \tag{4-4}$$

where u is the expansion velocity of the spouting particles, m_0 is the mass of the insulator, E_a is the energy used to accelerate the spouting particles. Letting E_a be E_L-E_t, the force F_2 as the reaction of the spouting particles is expressed by

$$F_2 = \frac{2}{u} \cdot \frac{E_L - E_t}{\tau}. \tag{4-5}$$

(3) Deduction of force F_3 in region 3

The intensive air breakdown plasma is observed in front of the surface of the insulator besides the plasma spouting from the surface of the insulator in this region. Therefore both the reaction of the spouting particles and the shock wave from the air breakdown plasma are considered as the vibration force of the insulator. Only the latter process is estimated here.

Assuming that the air breakdown plasma is momentarily generated at one special point in air where the whole laser beam energy is absorbed, the following equation expresses R_B which represents the radius of the spherical shock wave at the time t after the irradiation of the laser beam[32)]:

$$R_B = \xi_0 \left[\frac{E_L t^2}{\rho_0} \right]^{1/5}, \tag{4-6}$$

where $\xi_0 = [75(\gamma-1)(\gamma+1)/16\pi(3\gamma-1)]^{1/5}$, γ is the ratio of specific heat of the gas(=1.3 in air at atmospheric pressure), and ρ_0 is the density of air. The front pressure of the shock wave, P_3, is expressed by[32)]

$$P_3 = \frac{2\rho_0}{\gamma+1} \left[\frac{dR_B}{dt} \right]^2 = \frac{8}{25(\gamma+1)} \xi_0^2 (\rho_0^3 E_L^2 t^{-6})^{1/5}. \tag{4-7}$$

The variable t is eliminated using Eqs. (4-6) and (4-7), then the force F_3 on the surface is expressed by the following equation, integrating the normal line component in the pressure applied on the infinitely small ringed area, x in diameter and Δx in width, as shown in Fig. 4. 7:

$$F_3 = \frac{8\xi_0 E_L}{25(\gamma+1)} \int_0^{x'} \frac{2\pi r x}{(r+x^2)^2} dx, \tag{4-8}$$

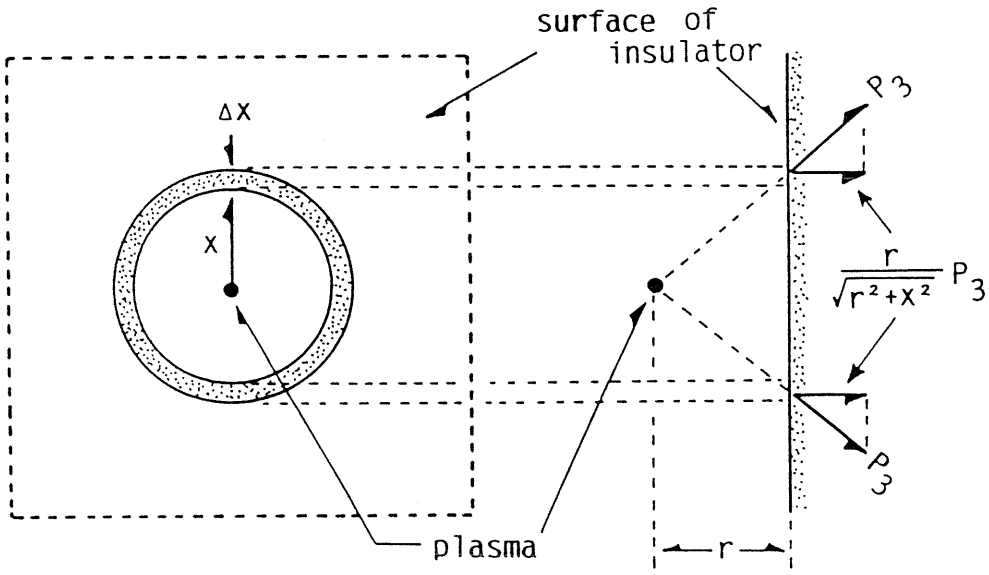

Fig. 4. 7. Relationship between location of laser-produced plasma and pressure P_3 on the surface of insulator.

where r is the distance between the air breakdown plasma and the surface of the insulator.

The relation between r and d is experimentally expressed by the following equation from the figure of the photographs as shown in Fig. 4. 2:

$$r \fallingdotseq \frac{d_{opt} + d - f}{2} . \tag{4-9}$$

Therefore, letting x' be infinite and substituting Eq. (4-9) into Eq. (4-8), the force F_3 is expressed by

$$F_3 = \frac{16\pi\xi_0 E_L}{25(\gamma + 1)(d_{opt} + d - f)} . \tag{4-10}$$

(4) Relative comparison of calculated forces with observed values of a_{rms}

Table 4. 1 shows the material constants of the insulator used for the calculation. The symbol '*' in Table 4. 1 is added to an unknown material constants, and the unknown constants are assumed to be the average of the material constants of Al_2O_3 and SiO_2. Quoting the expansion velocity of the atoms of Al, Si and O, contained chiefly in the insulator, from ref.30, the average of these velocities, 3×10^6 cm/s, is used for the calculation as the expansion velocity u. The mass m is estimated as about 2 μg/shot from the result of another experiment, corresponding to approximately to the value reported by Shimomura et al.[30]. However, the second term in Eq. (4-3) is much less than the first term, so that the energy loss E_t almost depends on the first term.

Table. 4. 1. Material constants for calculation.

thermal expansion coefficient	β = 5x10^{-6}(1/℃)
molecular weight*	M = 81
density	ρ = 2700(kg/m^3)
specific heat	C = 54.4(J/mol)
modulus of elasticity	ε = 1.0x10^{11}(N/m^2)
melting point*	Tm = 2000(K)
boiling point*	Tb = 3250(K)
latent heat of fusion*	Cm = 1.0x10^5(J/mol)
latent heat of evaporization*	Cb = 1.2x10^6(J/mol)
heat conductivity	K = 20(W/m·℃)

Fig. 4. 8 shows the relative variations of the calculated value F_2 and the observed value of a_{rms} at $d=d_{opt}$ with the change of the laser beam energy E_L as the standard that the relative values of a_{rms} and F_2 at E_L=5.9 J are 10. The variation of a_{rms} considerably agrees with the variation of F_2, and F_2 is nearly proportional to E_L because E_t is small compared with E_L. The same tendency is obtained in the variations of F_1 and F_3 with E_L. Therefore it is found that the dependence of a_{rms} on E_L can be explained using this model.

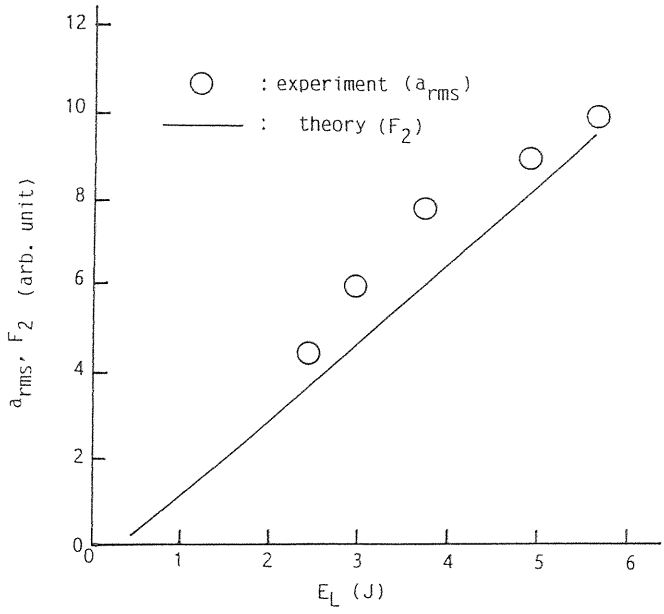

Fig. 4. 8. Relative variations of acceleration a_{rms} and force F_2 at $d=d_{opt}$ with laser energy E_L.

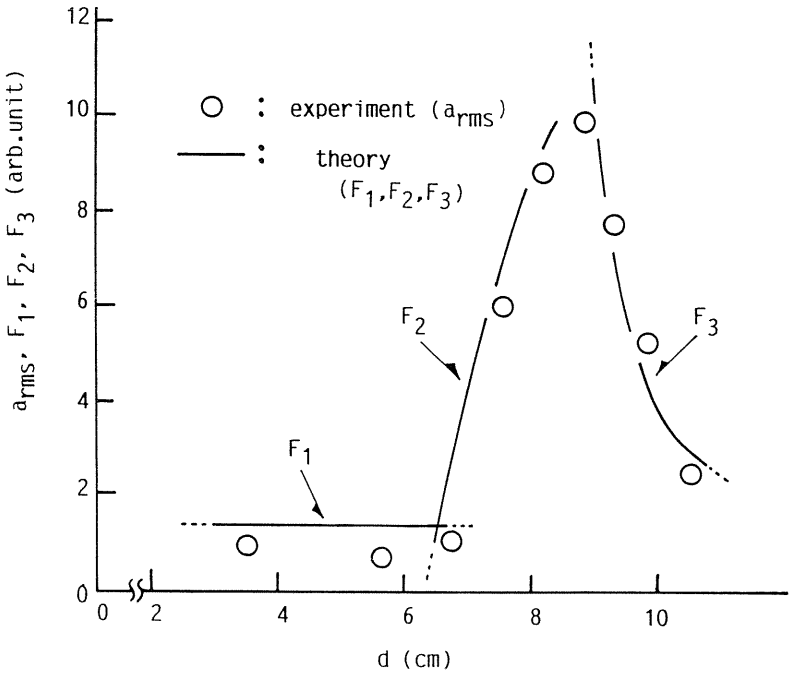

Fig. 4. 9. Relative variation of acceleration a_{rms} and forces F_1, F_2 and F_3 with d.

Fig. 4. 9 shows the relative variations of the observed value of a_{rms} and the calculated values of F_1, F_2 and F_3 with the change of d as the standard that the relative values of a_{rms} and F_2 at $d=d_{opt}$ are 10. The variation of a_{rms} with d in the three regions are found to be similar to those of F_1, F_2 and F_3, respectively.

From the above calculated results, it is found that the dependence of the vibrational amplitude on the laser beam energy E_L and the distance d can be explained by the model combining the thermal shock, the reaction of the spouting particles and the spherical shock wave from the air breakdown plasma. If the material constants of the insulator are known, the relative variation of the vibrational amplitude will be predicted.

5. Study on Non-Destructive and Remote Inspection of Electric Suspension Insulator by Means of Laser Beam

5. 1. Experimental Apparatus and Procedure

The vibration of an electric suspension insulator made of ceramics is measured using the apparatus shown in Fig. 4. 1, and the difference of the natural vibration between a normal insulator and a cracked one is observed for three kinds of the insulators whose diameters are about 26 cm, 28 cm and 30 cm, performing FFT to the vibrational signals. The estimation of the vibrational difference described in 5. 2. 2 is performed for several insulators 26 cm in diameter.

5. 2. *Experimental Results*

5. 2. 1. *Influence of Crack on Vibrational Spectrum of Electric Suspension Insulator*

Here is observed the vibrational difference between normal and cracked insulators for three kinds of the insulators with the diameters of about 26 cm, 28 cm and 30 cm. The artificial cracking of the insulator is performed by striking with a chisel, and the cracked insulator has one crack from the most inner rib to the periphery through the thickness of the whole shed. The typical crack found in an actual transmission line is obtained in such a way.

Fig. 5. 1 shows the temporal variation of the frequency spectrum of the natural vibration detected by the He-Ne laser interferometer for the cracked insulator 26 cm in diameter which is the same type as the insulator used in the chapter 4. The vibrational signal during 1—31 msec includes many frequency components similarly to the spectrum for the normal insulator shown in Fig. 4. 4. However, the frequency components of the natural vibration are not observed because the natural vibration decays so fast to a degree of background noise within the duration of 70 msec after the irradiation of the CO_2 laser beam. A similar tendency is observed for the insulator 28 cm in diameter as shown in Fig. 5. 2. Fig. 5. 3 shows the temporal variations of the frequency spectrums for the normal and cracked insualtors with the diameter of 30 cm. In the spectrum of the normal insulator, the frequency components of the natural vibration are observed at about 1.3 kHz and 2.6 kHz. However, the frequency components of the natural vibration shifts to the lower frequency of 0.9 kHz and 1.8 kHz in the spectrum for the cracked insulator. Furthermore, the amplitude of the natural vibration in the cracked insulator decays to a degree of background noise faster than that in the normal insulator.

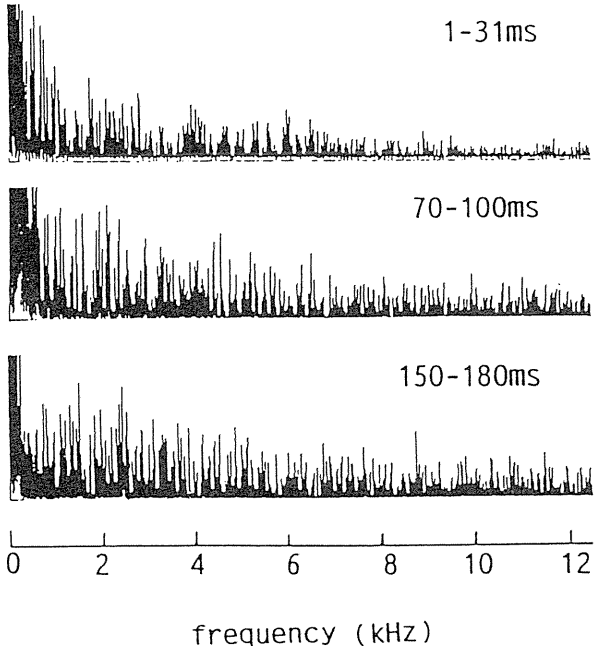

Fig. 5. 1. Temporal relative variation of vibrational frequency spectrum for a cracked insulator 26 cm in diameter.

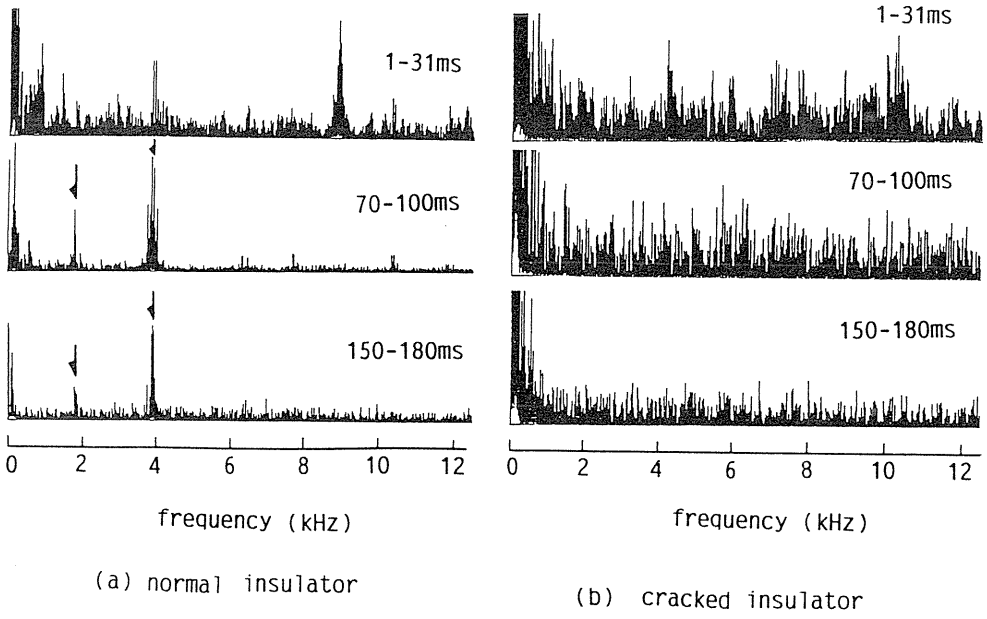

Fig. 5. 2. Temporal relative variations of vibrational frequency spectrums (a) for normal insulator and (b) for cracked insulator 28 cm in diameter.

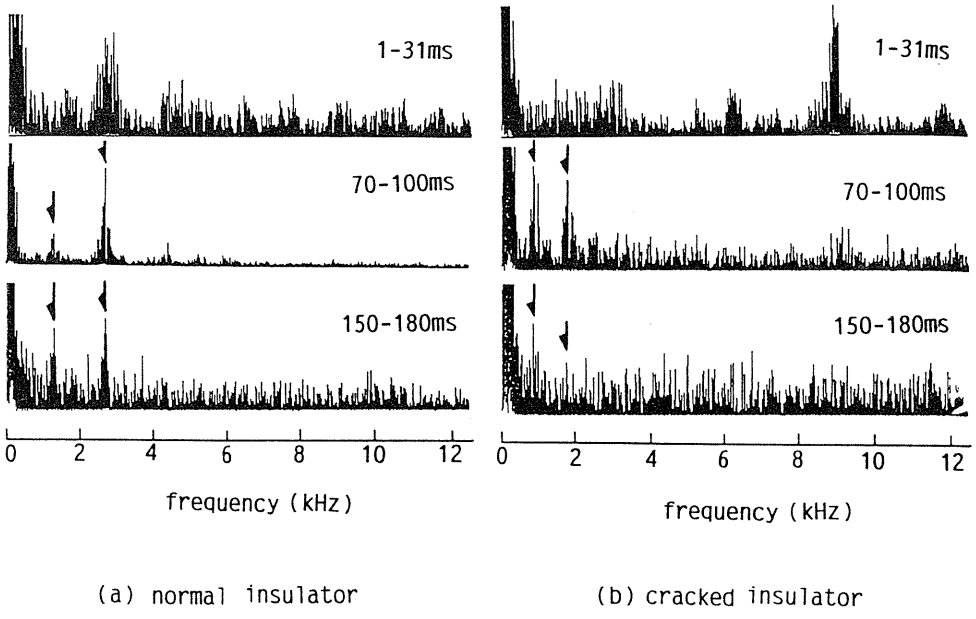

Fig. 5. 3. Temporal relative variations of vibrational frequency spectrums (a) for normal insulator and (b) for cracked insulator 30 cm in diameter.

From these observation, it is clear that the cracking of the insulator results in changing the natural vibration, and it is probable that the change of the natural vibration can be detected using a frequency analyzing technique.

5. 2. 2. Inspection of Electric Suspension Insulator

The inspection of the electric suspension insulator 26 cm in diameter is examined here. To distinguish a cracked insulator from a normal one, the detection of the vibrational changes is tried here by using frequency analyzing technique and by hearing the sound of the vibrational signal.

(1) Method to use frequency spectrum of natural vibration

It is tried to detect the cracked insulator by estimating the differences of vibrational frequency spectrum and the damping factor for the natural vibration at 4.4 kHz shown in Fig. 4. 4.

First, the method to estimate the difference of vibrational frequency spectrum is described. The difference is estimated in the spectrum during 150—180 msec after the irradiation of the CO_2 laser beam when the insulator is sufficiently vibrated in the natural mode. The standard spectrum $S_0(f)$ is defined as the average of the spectrums of three normal insulators normalized with the peak value at 4.4 kHz. As shown in Fig. 5. 4, the difference between the standard spectrum $S_0(f)$ and the spectrum S(f) of the inspected insulator is estimated by the integrated value V expressed by

$$V = \int_{f_0}^{f_1} \{S_0(f) - S(f)\}^2 \, df, \tag{5-1}$$

where f_0 is 3.9 kHz and f_1 is 4.9 kHz.

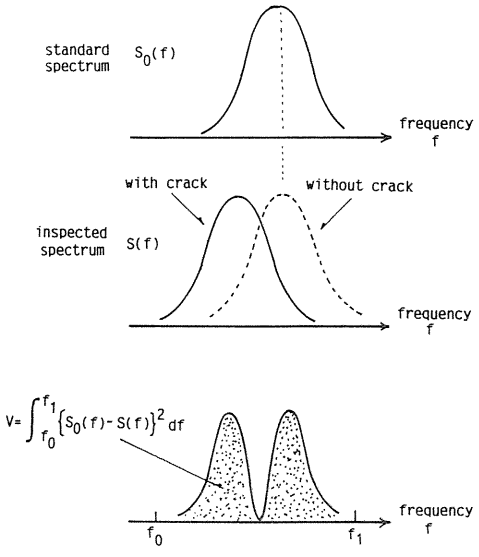

Fig. 5. 4. Estimation of spectrum difference.

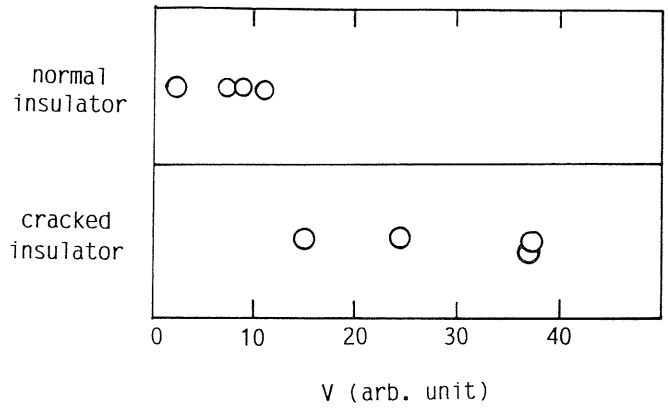

Fig. 5. 5. Change of difference to the standard spectrum due to crack.

Fig. 5. 5 shows the values V for the insulators with and without a crack. It is evident that the crack in the insulator causes the value of V to be increased, and the threshold for the distinction of a cracked insulator is estimated as the relative value of 12.

Next, the method to estimate the damping factor of the natural vibration is described. The damping factor k is defined by the following equation which expresses the intensity I of the natural vibration at the time t:

$$I = I_0 \cdot exp(-kt)\,, \tag{5-2}$$

where I_0 is a constant value.

Fig. 5. 6 shows the values k for the insulators with and without a crack. It is apparent that the crack in the insulator causes the value of k to be increased, and the threshold of k for the distinction of a cracked insulator is estimated as about 11 sec^{-1}.

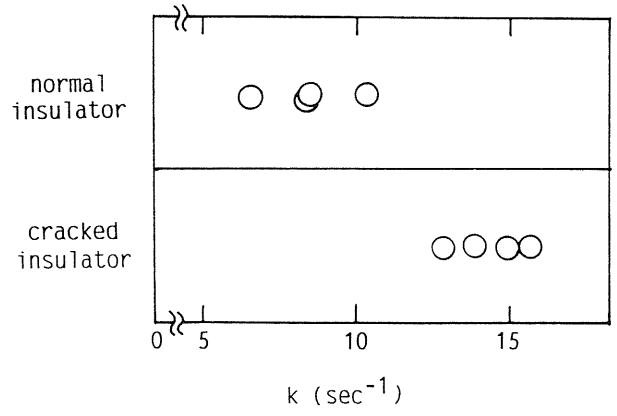

Fig. 5. 6. Change of damping factor k of vibration due to crack.

(2) Method to hear the sound of vibrational signal

The vibrational signal detected by the laser interferometer is recorded with a tape recorder, and the sound of the signal is carefully heard. It is possible to distinguish the cracked insulator by hearing the sound of the vibrational signal because the sound of the signal is similar to the sound caused by slightly striking the insulator with a metal rod.

Although the obscurity of the judgment remains in this method, the hearing of the vibrational signal is considered to be an economic method because a human can recognize the slight difference of the sound for frequency and damping time without the expensive instruments like a FFT analyzer.

(3) Application of these methods to practical uses

Although it is necessary to examine the reliability, especially the accuracy of the judgment, by testing many various insulators, it is suggested that the cracked insulator can be distinguished by using the vibrational frequency spectrum and by hearing the sound of the vibrational signal detected with a laser interferometer. The combination of these methods is expected to make the inspection more reliable. Further these methods are properly used according to the inspecting conditions. It is considered that the method to hear the sound of vibrational signal is preferable for an inspection in an actual field spot because of the needlessness of expensive instruments and that the method to use the vibrational spectrum is preferable for an automatic inspection in a production line or a field.

Although the inspection has been performed only for the insulator 26 cm in diameter, it is considered that the insulators with different diameters of 28 cm and 30 cm can be also inspected because the change of the natural vibration is clearly observed.

5. 2. 3. Irradiation Intensity of Laser Beam to Inspect Electric Suspension Insulator

It is examined if the frequency spectrum of the natural vibration as shown in Fig. 4. 4 is observed with the change of the irradiation intensity of laser beam for the insulator 26 cm in diameter. From the results shown in Fig. 5. 7, it is obvious that the frequency spectrum of the natural vibration is observed for the irradiation intensity over 2×10^7 W/cm^2. This value considerably agrees with the irradiation intensity where a plasma spouts from the surface of the insulator as shown in Fig. 4. 6. A similar tendency is also observed for the insulators 28 cm and 30 cm in diameter.

5. 3. Perspective for Long Distant Inspection of Electric Suspension Insulator

It is suggested from the results in 5. 2. 2 that the cracked insulator can be remotely distinguished from the distance of about 10 cm, corresponding to the focal length of the convex germanium lens. Here are examined the conditions to inspect the insulator from a long distance of several-tens meter using the method described in 5. 2. 2 at the standpoint of the irradiation intensity of laser beam.

When the laser beam with TEM_{00} mode is focussed through a convex lens with the focal length of f, the beam radius w_{02} at the beam waist, where the radius of the focused laser beam is minimum, and the distance z between the lens and the beam waist satisfy the following equations[33]:

$$z = f - \frac{f^3}{f^2 + (\pi w_{01}/\lambda)^2}, \tag{5-3}$$

$$\frac{1}{w_{02}} = \frac{1}{w_{01}} + \frac{(\pi w_{01}/\lambda)^2}{f^2}, \tag{5-4}$$

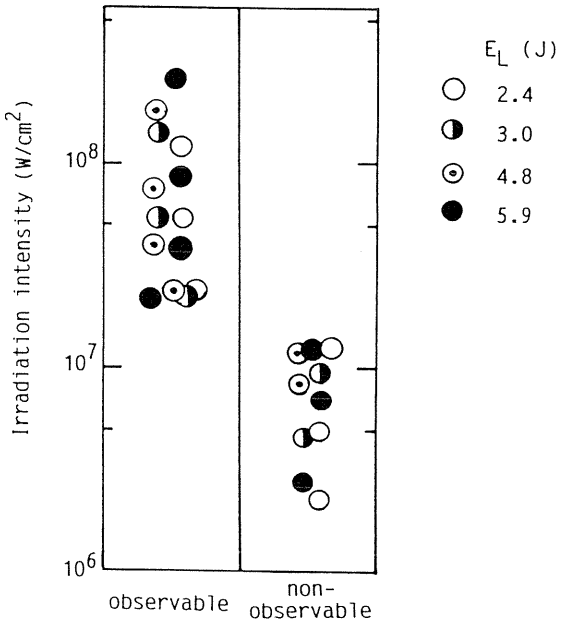

Fig. 5. 7. Observation of natural vibration with change of irradiation intensity of laser beam.

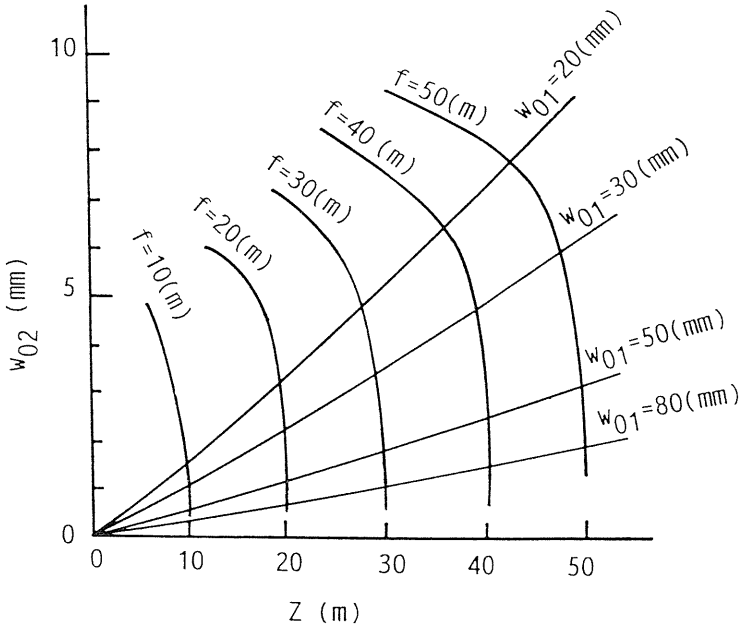

Fig. 5. 8. Contour lines of focal length f and incident beam radius w_{01} as function of distance z and beam radius w_{02} at beam waist.

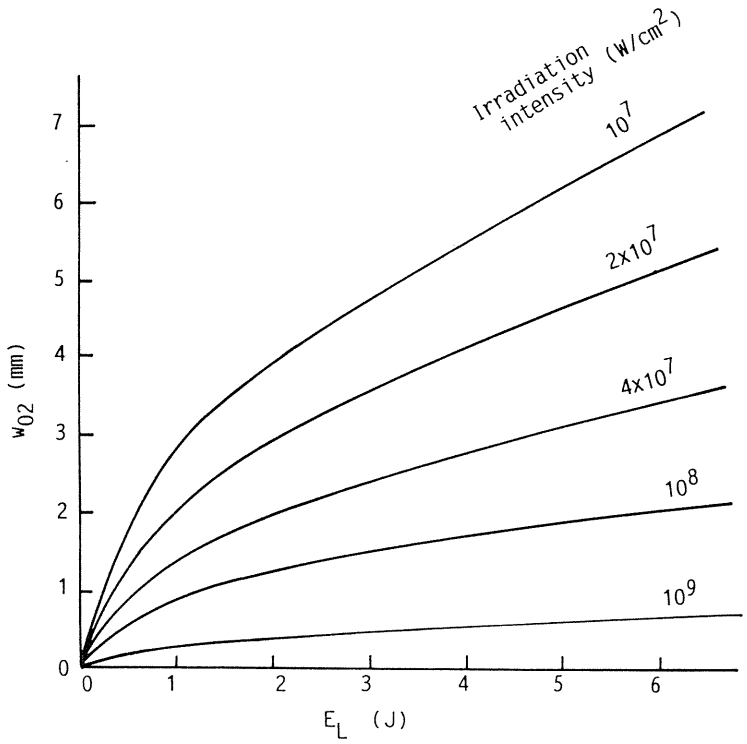

Fig. 5. 9. Relationship between laser beam energy E_L and beam radius w_{02} at beam waist as a parameter of irradiation intensity of laser beam.

where w_{01} is the beam radius before the incidence into the lens, and λ is the wavelength of CO_2 laser beam. Fig. 5. 8 shows the contour lines of f and w_{01} as functions of W_{02} and z, resolving Eqs. (5-3) and (5-4).

Fig. 5. 9 shows the relationship between the laser beam energy E_L and the beam radius W_{02} at the beam waist, assuming that the pulse width of the laser beam is 400 nsec.

The procedure to determine w_{01} and f in the case that the insulator is inspected from the distance of z using a pulsed CO_2 laser beam with the energy of E_L is described below. To make the explanation simple, the values of z and E_L are let be 40 m and 2 J, respectively. As the irradiation intensity over 2×10^7 W/cm^2 is necessary at least to inspect the insulator, the radius w_{02} has to be less than 3 mm from Fig. 5. 9. Letting w_{02} to be 3 mm, the values of f and w_{02} are about 40 m and 45 mm, respectively, in accordance to the contour lines shown in Fig. 5. 8.

Such a laser device and a convex lens can be produced technically, and it has been reported to generate the air breakdown plasma longer than 20 m along the direction of the laser beam with a convex lens whose focal length is 30 m[34]. Further the interferometer measuring system with the resolving power of several-ten nano-meter from a 100 m distance has been also reported[35)-40)], and this system has a good ability enough to detect the natural vibration of the insulator. Therefore, it is suggested that the insulator can be inspected from a several-tens-meter distance.

In a field inspection, it is necessary to avoid the influence of wind on the measuring system. As the swing of the insulator due to wind induces a continuous change in the output signal of the interferometer, the choice of the natural vibration not to overlap on the continuous change in frequency region leads to the avoidance of the influence of the swing. Further a pulsive disturbance can be avoided by operating the pulsed laser in a proper timing.

6. Conclusion

Discharge-pumped pulsed CO_2 lasers are powerful far-infrared coherent sources and have the various potential applications in science and industry. From a practical point of view, it is desirable to increase the extractable energy in a corona-preionized compact TEA-CO_2 laser, because an efficient laser operation is possible with an easy maintenance. In this thesis, the superposition of a high frequency corona discharge (called as HFCD) on a main discharge was focussed on in order to increase the laser output. Additionally, the non-destructive and remote inspection of electric suspension insulators was tried as an application of pulsed CO_2 laser.

First of all, the superposition of the HFCD on the main discharge was examined in order to increase the preionization intensity in a corona-preionized TEA-CO_2 laser. The laser output was increased by this method for the input energy density up to about 220 J/l, where the laser output was saturated due to the glow-to-arc transition in an ordinary corona-preionized TEA-CO_2 laser, and the maximum laser output density of about 14 J/l was obtained. When the HFCD current was characterized by the triggering time ($t_{G3\text{-}BD}$), the peak value (I_p), the half period (T) and the duration (t_c), the optimization of $t_{G3\text{-}BD}$, the increase of I_p and the decrease of T were necessary to increase the laser output, while t_c was required to be more than about 1 μs. It was considered that homogeneous electron layers should be produced by the HFCD current while the discharge current flowed from the peaking capacitor C_2. On the other hand, it was also considered that the increase of the peak value and the decrease of the half period led to the suppression of the glow-to-arc transtion because the electron density of the layer was increased with the peak value of the HFCD current and the production rate of the layer was increased with the decrease of the half period. Furthermore, when the triggering time of the HFCD current was optimized to maximize the laser output, the delay time of the main discharge after flowing the HFCD current corresponded to the time required for the layer to propagate across the main electrodes. That suggested that the glow-to-arc transition was effectively suppressed after the whole discharge volume was sufficiently ionized by the electron layer. It was also suggested from the calculation using the equivalent circuit that the reductions of resistance and inductance in the HFCD circuit might result in increasing the laser output.

A new HFCD circuit without another power source (called as SC-HFCD circuit) was devised to miniaturize the laser device and to save the energy for the HFCD operation. In the SC-HFCD circuit, the HFCD operation was possible by recycling the residual energy not to be injected into the discharge volume. Both the main discharge and the laser output were improved due to the HFCD effect using the SC-HFCD circuit, and glow discharges were produced for the input energy density up to 230 J/l after the main discharge circuit and the laser gas mixture were optimized. Moreover, the maximum laser output of 17.5 J/l was obtained with the SC-HFCD circuit at the input energy density of 250 J/l. The output voltage of the SC-HFCD circuit was determined by the amounts of electrical charge flowing into and out of the SC-HFCD circuit, and the output voltage was maintained at a constant value when those

two amounts of electrical charge were equal. The output voltage was decreased when the glow-to-arc transition occured, because the residual energy was not collected due to the rapid reduction of the voltage across the main electrodes. These charcteristics of the output voltage were predicted by the calculation using the equivalent circuit, and the observed and calculated results considerably agreed. The increase of the capacitance to collect the residual energy led to the insurance of the HFCD operation because the output voltage of the SC-HFCD circuit was maintained at a relatively high value even if the glow-to-arc transition should occur.

The vibration of the electric suspension insulator with the irradiation of a pulsed CO_2 laser beam was measured using an acceleration sensor and a laser interferometer. It was shown that the vibration included many various frequency components immidiately after the irradiation of the laser beam and that the insulator continued to be vibrated in the natural mode after passing time. The irradiation intensity had much effect on both the vibrational amplitude and the phenomena on the surface of the insulator. The change of the vibrational amplitude corresponded to that of the phenomena. These changes with the irradiation intensity were composed of following three regions. In the region 1, the laser-produced plasma was seldom observed on the surface of the insulator and the vibrational amplitude was independent of the irradiation intensity. In the region 2, the intensive plasma spouting from the whole spot area was observed and the vibrational amplitude was increased with the irradiation intensity. In the region 3, the air-breakdown plasma was observed in front of the surface of the insulator other than the plasma spouting from the spot area, and the vibrational amplitude was decreased with the irradiation intensity. Assuming that the dominant vibration force in each region was the thermal shock, the reaction of the spouting particles and the spherical shock wave from the air-breakdown plasma, respectively, the calculated variation of the force applied on the surface of the insulator relatively agreed with the observed variation of the vibrational amplitude.

The non-destructive and remote inspection of an electric suspension insulator by measuring the natural vibration was described. Furthermore, the conditions to apply this technique to the actual field inspection on the transmission line tower was investigated. It was suggested from the results of the frequency analysis that the frequency components and the decay constant of the natural vibration changed due to a crack independently of the size of the insulator. Therefore the influences of cracks on the frequency components and the decay constant of the natural vibration were estimated by both the quantitative method using the frequency analysis and the sensoring method using the human's auditory sense. It was shown that the cracked insulator was distinguished by these two methods under the condition of the irradiation intensity of the pulsed CO_2 laser over 2×10^7 W/cm^2, and that the condition of the irradiation intensity was attained with a comparative ease using the present laser technology evenwhen the pulsed CO_2 laser beam was irradiated on the surface of the insulator from the distance of several-tens meter. Therefore it was considered that the inspection described here will be applied to the actual field. Moreover, it was considered that the influence of wind on the inspection system can be avoided by operating the pulsed laser in a proper timing and by choosing the proper natural-mode spectrum.

Acknowledgements

The authors would like to express our gratitude to the members of NGK INSULATOR, LTD. for their cooperation and the supply of the insulators. The authors are also grateful to the colleagues and the students who collaborated with us in each work.

References

1) R. Marchetti, E. Penco and G. Salvetti: "Sealed, miniaturized, corona-preionized, high-repetition-rate TEA CO_2 laser using hydrogen buffered gas mixtures", IEEE J. Quantum Electron. QE-21(1985) 1766.
2) G.J. Ernst: "Single-frequency, atmospheric pressure CO_2 laser", Rev. Sci. Instrum. 48(1977) 1281.
3) G.J. Ernst and A.G. Boer: "Construction and performance characteristics of a rapid discharge TEA CO_2 laser", Opt. Commun. 27(1978) 105.
4) G.J. Ernst and A.G. Boer: "A 5 cm single-discharge CO_2 laser having high power output", Opt. Commun. 34(1980) 221.
5) G.J. Ernst: "A 10 cm aperture, high quality TEA CO_2 laser", Opt. Commun. 44(1982) 125.
6) G.J. Ernst: "Uniform-field electrodes with minimum width", Opt. Commun. 49(1984) 275.
7) C. Yamabe, H. Ishihara, H. Akiyama and K. Horii: "Improvement of laser output of TEA CO_2 laser by high frequency corona discharge", Rev. Laser Eng. 14(1986) 960.
8) A.C. Tam: "Applications of Photoacoustic sensing techniques", Rev. Mod. Phys. 58(1986) 381.
9) D.A. Hutchins: "Mechanisms of pulsed photoacoustic generation", Can. J. Phys. 64(1986) 1247.
10) J.A. Cooper, R.A. Crosbie, R.J. Dewhurst, A.D.W. Mckie and S.B. Palmer: "Surface acoustic wave interactions with cracks and slots: A non-contacting study using lasers", IEEE Trans. Ultrason. Ferroelect. and Freq. Cont. UFFC-33(1986) 462.
11) R.J. Dewhurst, D.A. Hutchins and S.B. Palmer: "Quantitative measurements of laser-generated acoustic waveforms", J. Appl. Phys. 53(1982) 4064.
12) P. Hess and J. Pelzl: Photo Acoustic and Photo Thermal Phenomena p400 (Springer Series in Optical Sciences vol.58, Springer-Verlag, Berlin, Heidelberg, New York, London, Paris, Tokyo)
13) K. Hane, T. Kanie and S. Hattori: "Photothermoelastic probing for a clamped plate sample", Appl. Opt. 27(1988) 386.
14) I. Tomeno and H. Ohzu: "Photoacoustic signal from subsurface defects in ceramics", Jpn. J. Appl. Phys. 24(1985) 1445.
15) P. Cielo: "Pulsed photothermal evaluation of layered materials", J. Appl. Phys. 56(1984) 230.
16) T.Y. Chang: "Improved uniform-field electrode profiles for TEA laser and high-voltage applications", Rev. Sci. Instrum. 44(1973) 405.
17) H. Akiyama, T. Takamatsu, C. Yamabe and K. Horii: "Suppression of glow-to-arc transition in atmospheric pressure gas discharge of TEA CO_2 laser by high frequency corona discharges", J. Phys. E: Sci. Instrum. 17(1984) 1014.
18) H. Shields, J. Giannelli and A.L.S. Smith: "X-ray preionized CO_2 laser", Appl. Phys. B 37(1985) 219.
19) M.C. Richardson, A.J. Alcock, K. Leopold and P. Burtyn: "A 300-J multigigawatt CO_2 laser", IEEE J. Quantum Electron. QE-9(1973) 236.
20) M.C. Richardson, K. Leopold and A.J. Alcock: "Large Aperture CO_2 laser discharges", IEEE J. Quantum Electron. QE-9(1973) 934.
21) A.J. Palmer: "A physical model on the initiation of atmospheric-pressure glow discharges", Appl. Phys. Lett. 25(1974) 138.
22) J.I. Levatter and S. Lin: "Necessary conditions for the homogeneous formation of pulsed avalanche discharges at high gas pressures", J. Appl. Phys. 51(1980) 210.
23) J.J. Lowke, A.V. Phelps and B.W. Irwin: "Predicted electron transport coefficients and operating characteristics of CO_2-N_2-He laser mixtures", J. Appl. Phys. 44(1973) 4664.
24) S. Sato, C. Yamabe and K. Horii: "An analysis of the laser output properties for a TEA CO_2 laser with the design of experiments", Trans. IEE Jpn. 100-A(1980) 657, in Japanese.
25) R. Marchetti, E. Penco and G. Salvetti: "Sealed, miniaturized, corona-preionized, high-repetition-rate TEA-CO_2 laser using hydrogen buffered gas mixtures", IEEE J. Quantum Electron. QE-21(1985) 1766.
26) G.J. Ernst: "A 10 cm aperture, high quality TEA CO_2 laser", Opt. Commun. 44(1982) 125.

27) O.P. Judd and J.Y. Wada: "Investigations of a UV preionized electrical discharge and CO_2 laser", IEEE J. Quantum Electron. QE-10(1974) 12.
28) P.E. Dyer and D.N. Raouf: "Axial X-ray preionization of a 10 atmosphere pressure TE CO_2 laser", Opt. Commun. 53(1985) 36.
29) L.S. Gournay: "Conversion of electromagnetic to acoustic energy by surface heating", J. Acoust. Soc. Am. 40(1966) 1322.
30) T. Shimomura, M. Yano, T. Noguchi and K. Horii: "Laser-produced metal plasma", Bulletin of the Electro-technical Laboratory, 36(1972) 264, in Japanese.
31) C. Yamanaka: REZA-KOGAKU p163 (Denki denshi kogaku taikei, No.20, 1981, CORONA-sha), in Japanese.
32) Y.B. Zel'dovich and Y.P. Raizer: Physics of Shock Waves and High-Temperature Hydrodynamic Phenomena, p99 (Academic Press, New York and London, 1966)
33) T. Takaoka and T. Takahashi: REZA-GIJUTSU-NYUMON p87 (1986, AKIBA-shuppan), in Japanese.
34) W.F. Hagen: "Diffraction-limitted high-radiance Nd-glass laser system", J. Appl. Phys. 40(1969) 511.
35) K.M. Baird: "The role of interferometry in long distance measurement", Metrologia, 4(1968) 135.
36) G.L. Bouldet and A.G. Orszag: "Absolute distance measurements by CO_2 laser multiwavelength interferometry", Appl. Opt. 18(1979) 225.
37) C.W. Gillard, N.E. Buholz and D.W. Ridder: "Absolute distance interferometry", Opt. Eng. 20(1981) 129.
38) H. Matsumoto and S. Seino: "Infrared two-wavelength interferometry for measuring long length", Ann. CIRP, 31(1982) 401.
39) H. Matsumoto: "Synthetic millimeter-wave signal generation for length measurement", Appl. Opt. 23(1984) 973.
40) H. Matsumoto: JIDOKA-GIJUTSU p26, vol.17, No.10 (1985), in Japanese.